scientific reports

Check for updates

OPEN

Robust post-processing time frequency technology and its application to mechanical fault diagnosis

Junbo Long[1], Changshou Deng[1]✉ & Haibin Wang[2]

Post-processing synchrosqueezing transform and synchroextracting transform methods can improve TFR resolution for fault diagnosis. The normal and fault signal can be described by infinite variance process, and $1 < \alpha \leq 2$, even the background noise belongs to the process under complex conditions. The effect of traditional SST and SET methods is greatly reduced and even lost in infinite variance process environment. Several robust post-processing methods are proposed including FSET, FSSET, FSOSET and FMSST technology employing infinite variance process statistical model and FLOS, and their mathematical derivation are completed in this paper. The proposed methods are compared with the conventional methods, and the results show that the proposed methods achieve better results than the existing methods. In addition, the new methods are applied to diagnose the bearing outer race DE signals polluted by infinite variance process, the result demonstrates that they have performance advantages. Finally, the characteristics, shortcomings and application scenarios of the improved algorithms are summarized.

Keywords Infinite variance process, Synchrosqueezing extracting, Fuzzy energy, Feature extraction, Multi-synchrosqueezing

Abbreviations

SST	Synchrosqueezing transform
SET	Synchroextracting transform
TFR	Time-frequency representation
FSET	Fractional low order synchroextracting transform
FSSET	Fractional low order synchrosqueezing extracting transform
FSOSET	Fractional low order second-order synchroextracting transform
FMSST	Fractional low order multi-synchrosqueezing transform
FLOS	Fractional low order statistics
TF	Time-frequency
FSTFT	Fractional lower order short-time Fourier transform
FWVD	Fractional lower order Wigner–Ville distribution
FSST	Fractional lower order synchrosqueezing transform
FST	Fractional lower order S transform
PDF	Probability density function

Mechanical bearing is an important part of rotating machinery, and the failure of bearing is one of the main causes of mechanical damage. Therefore, real-time supervision of the rotating machinery equipment is an important means to ensure labor and production, which has become a current research hotspot[1–3]. Time–frequency representation can accurately reflect the three-dimensional relationship between frequency, time and amplitude, and which is an effective tool for analyzing the vibration signals[4–6].

The energy aggregation of TFR will directly affect the performance of mechanical bearing fault feature extraction. Due to Cross term interference effect and Heisenberg's uncertainty principle, the classical TFR cannot achieve concentration in both time and frequency domains including STFT, CWT, and WVD technologies, and

[1]College of Electronic Information Engineering, Jiujiang University, Jiujiang, China. [2]College of Computer and Big Data Science, Jiujiang University, Jiujiang, China. ✉email: dengtju@aliyun.com

so on. Therefore, the synchrosqueezing and synchroextracting transform TFR methods have been proposed one after another including synchrosqueezing transform[7], synchrosqueezed wavelet transform[8], synchroextracting transform[9], synchrosqueezing S transform[4], and so on. The proposed methods can further improve the energy concentration of TFR, which have been widely used in various fields[10–12]. In order to obtain a more accurate TFR with a higher time–frequency concentration, above methods are extended to second-order or higher-order domains including second order multi-synchrosqueezing[13], second order transient extracting transform[14], second-order synchroextracting transform[15], high-order synchrosqueezing transform[16], high-order synchroextracting transform[17], and so on. Moreover, a synchrosqueezing extracting transform time–frequency analysis method combining synchrosqueezing and extracting transform was proposed to get a more concentrated TFR[18], which has been applied to analyze the bearing vibration signals under variable speed conditions. Compared with the SST method, RM is a method that reallocates both time and frequency of STFT TF results, which can improve the readability of TF representation[19]. The RM technique first calculates the new reallocation of each TF point based on the TF phase information. Then, the TF representation is integrated in the TF direction by a two-dimensional reassignment operation. RM technique shows that post-processing process of the traditional TF methods is an effective way to obtain clearer TF results. However, RM results cannot be used for time series signal reconstruction. In addition, aiming at the strong time-varying non-stationary signals, Chen et al. combined the iterative idea of second-order instantaneous frequency estimation and multiple synchronous compression transform to approximate the real instantaneous frequency trajectory, and proposed a second-order multi-synchronous compression transform, which has good performance in terms of signal time–frequency energy concentration and noise robustness[20]. Employing iterative reassignment technology, MSST improves the energy concentration of TF representation by applying multiple SST operation processes, which provides a better way for strong time-varying multi-component signals. Hence, MSST has good ability in TF energy concentration and noise signal suppression. In addition, for strong time-varying signals, Yu et al. proposed a new technique combining demodulation technology and synchronous extraction transform, which can accurately capture the rapidly changing dynamic information of the signals[21]. Ying et al. proposed a novel angle-time double-layer decomposition structure termed order-frequency Holo-Hilbert spectral analysis, the method is applied to the fault feature demodulation of variable vibration signals, which has higher fault recognition rate and stronger anti-noise ability[22]. The linear class STFT time–frequency method is limited by the Heisenberg–Gabor inequality, and the continuous wavelet transform (CWT) time–frequency method cannot obtain good resolution at the same time and frequency of the fault signal. Bilinear class WVD time–frequency method and its improved algorithm have better time–frequency resolution, but it is inevitably subject to cross term interference. Parametric model class methods have no cross term in time–frequency domain, but the calculation is large and the resolution is not high. Synchrosqueezing and synchroextracting class time–frequency method has high time–frequency concentration, but some algorithms are degraded seriously in the face of strong pulse process noise.

In a sense, the development of bearing fault signal analysis can be summarized by three "non" words including non-Gaussian, non-stationary and nonlinear. Literature[23–27] confirmed that PDF of most fault vibration signals has a certain trailing, which belongs to infinite variance process, and even the noise in the signal is also infinite variance process. The infinite variance process signal or noise have no finite second or higher order moments, and the above mentioned TFR methods based on Gaussian hypothesis may produce large error and even fail in the pulse process conditions. Hence, it is urgent to seek new solutions for the particular case.

For stable distributed pulse processes, some methods based on fractional lower order statistics have been proposed including fractional lower order linear chirplet transform, fractional lower order short-time Fourier transform TFR, fractional lower order Wigner–Ville distribution TFR, fractional lower order synchrosqueezing transform TFR, fractional lower order S transform TFR, parameter model class TFR methods for mechanical bearing fault diagnosis in complex environments[28]. Most of these methods use the infinite variance process model and introduce fractional low-order statistics instead of the traditional second-order statistics to improve the algorithm, which can suppress the infinite variance process noise and achieve good results, but the time–frequency energy concentration of these methods is not too high.

To further reduce the impact of pulse process in FSTFT TF domain and improve TF concentration of the fault signals, several robust SET-based and SST-based TFR methods are proposed including fractional low order multiple iterations synchrosqueezing transform, fractional low order synchroextracting transform, fractional low order synchrosqueezing extracting transform, fractional low order second-order synchroextracting transform and fractional low order multi-synchrosqueezing transform algorithms based on infinite variance process statistical model and FLOS. By comparing the results of the post-processing SET-based, SST-based TFR methods and the conventional methods under characteristic index $\alpha = 2$ and $\alpha = 0.8$ conditions, we can know that the proposed SST, SET, SSET, SOSET and MSST methods have lower IF estimation *MSEs* and Renyi Entropy, higher *MSNR* output in different *MSNR* and characteristic index α. Especially, when $\alpha < 1.6$, the advantage of the robust methods is more obvious. In practical applications, the robust post-processing FSET, FSSET, FSOSET and FMSST algorithms are applied to demonstrate the TF distributions of the fault signal position relative to load zone centered at 6:00 data polluted by α infinite variance process ($\alpha \leq 2$), the result shows that the fault characteristic frequency and main vibration frequency of the fault signal can be clearly revealed in the TF domain. Hence, the robust methods are feasible and effective for fault diagnosis.

Infinite variance process and fault signals

Infinite variance process

The infinite variance process is also called the α stable distribution process, and which gets its name because it has no finite second moment, the process can be described by characteristic functions

$$\phi(t) = \exp\left\{j\mu t - \gamma|t|^{\alpha}[1 + j\beta sign(t)\omega(\tau,\alpha)]\right\}, \quad (1)$$

where α, β, μ and γ are the characteristic index, symmetry parameter, position parameter and dispersion coefficient respectively. PDFs of α distribution are shown in Fig. 1 (α=0.5, 0.75, 1.0, 1.25, 1.5, 1.75 and 2.0) when $\mu = 0, \gamma = 1$ and $\beta = 0$. Figure 1 reveals that the pulse of the infinite variance process decreases with the increase of the feature index, and the PDF trailing becomes shorter.

Fault signals

The real bearing fault data are from the Case Western Reserve University bearing data center[29]. The dimensions of the fault gap is 0.021 inches, the sampling frequency of the collected signal is set as 48000Hz, and the motor speed is 1774 revolutions per minute (rpm). We apply the characteristic function of infinite variance process in Eq. (1) to calculate the parameters α, γ, μ and β of the normal and drive end bearing fault data, the results are shown in Table 1, and their vibration waveforms are given in Fig. 2 (One second of data is selected as the test signal). It can be seen that the values of the characteristic index α of the normal and ball fault data in DE and FE are equal to 2, so which belong to Gaussian distribution in the absence of failure (It can also be generalized to infinite variance process, $\alpha = 2$). However, the values of the characteristic index α of the inner race fault and outer race position relative to load zone centered at 6:00, orthogonal at 3:00 and opposite at 12:00 all have a value less than 2, which are lower order infinite variance process ($\alpha < 2$), and their vibration waveforms have a distinct pulsing character.

PDFs of the bearing normal data and drive end bearing fault data in Table 1 are shown in Fig. 3. It can be seen that PDFs of the bearing normal signal in DE and FE converge at $x = 0.3$, and PDFs of the ball data are equal to 0 about at $x = 0.4$ and $x = 0.7$. But the bearing inner race and outer race data have long trails, in particular, the outer race fault signals have not fully converged at $x = 4$ yet, and their pulse properties are remarkable.

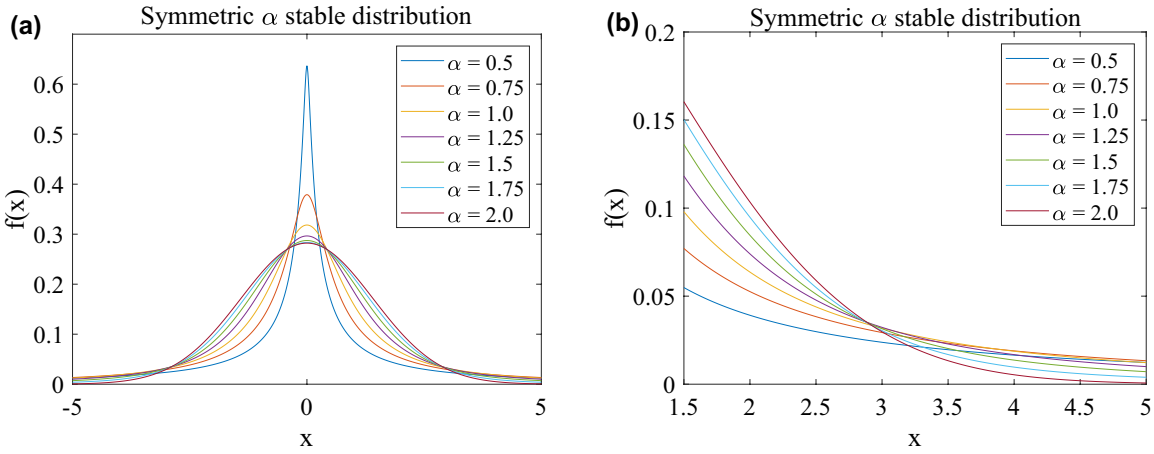

Figure 1. PDFs of infinite variance process ($\mu = 0, \gamma = 1$ and $\beta = 0$, α=0.5, 0.75, 1.0, 1.25, 1.5, 1.75 and 2.0).

Fault type		Measurement point	Infinite variance process parameters			
			α	β	γ	μ
No fault		DE	2.0	−1	0.0452	0.0136
		FE	2.0	0.9365	0.0485	0.031
Inner race fault		DE	1.8883	−0.1190	0.4030	0.0061
		FE	1.7119	0.1119	0.1241	0.0318
Ball fault		DE	2.0	0.3951	0.1208	0.0086
		FE	2.0	0.3957	0.0587	0.0296
Fault position	Centered at 6:00	DE	1.1559	−0.0162	0.1393	0.0110
		FE	1.4784	−0.0497	0.0905	0.0289
	Orthogonal at 3:00	DE	1.4039	0.0784	0.3544	0.0353
		FE	1.5435	0.0354	0.1256	0.0361
	Opposite at 12:00	DE	1.1584	−0.0149	0.1256	0.0167
		FE	1.6424	−0.0526	0.0732	0.0308

Table 1. Infinite variance process parameters of the fault signals.

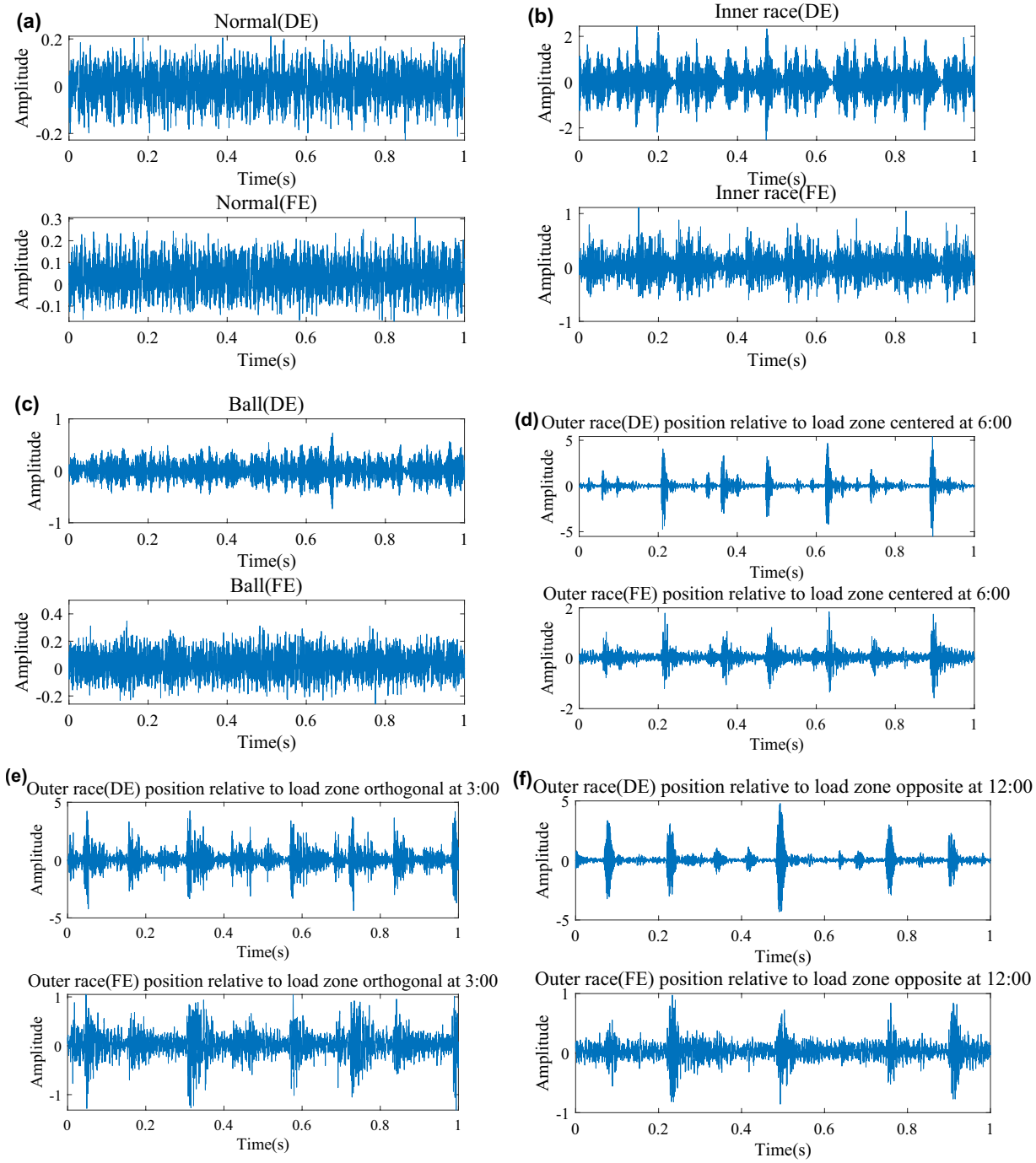

Figure 2. The vibration waveforms. (**a**) Normal; (**b**) inner race fault; (**c**) ball fault; (**d**) outer race fault at 6:00; (**e**) outer race fault at 3:00; (**f**) outer race fault at 12:00.

Robust post-processing TFR technologies

FSSET method

Principle

For an analytical signal $x(\tau) \in L^1(R)$, its FLO short time Fourier transform (FSTFT) with respect to the window is given by

$$FLOSTFT_x(t,\omega) = \int_{-\infty}^{+\infty} x^{<p>}(\tau) h(\tau - t) e^{-j\omega\tau} d\tau, \tag{2}$$

where t and τ is the time parameter, $h(\tau - t)$ is a differentiable analysis window function. $< p >$ denotes fractional p order moment of $x(\tau)$, $x^{<p>}(\tau) = |x(\tau)|^{p+1}/x^*(\tau), 0 < p \leq \alpha/2$.

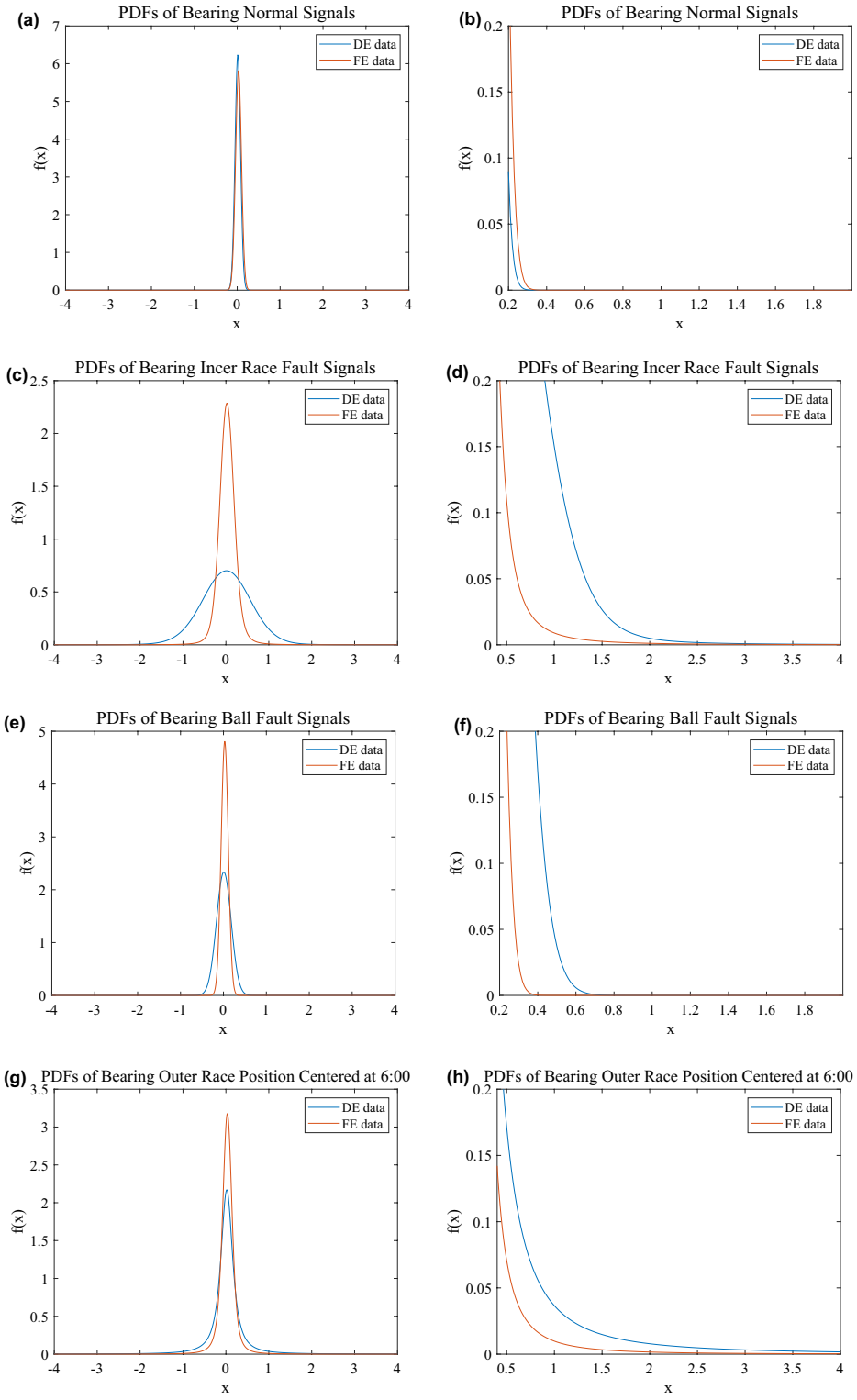

Figure 3. PDFs of the vibration signals. (**a,b**) Normal; (**c,d**) inner race; (**e,f**) ball; (**g,h**) outer race position relative to load zone centered at 6:00; (**i,j**) outer race at 3:00; (**k,l**) outer race at 12:00).

Aimming at α stable distributed environment, according to the concept of SST in Ref.[7], FSST can be defined as

$$FLOSST(t,\eta) = \int_{-\infty}^{+\infty} FLOSTFT_e(t,\omega) \cdot \delta[\eta - \varpi(t,\omega)]d\omega, \tag{3}$$

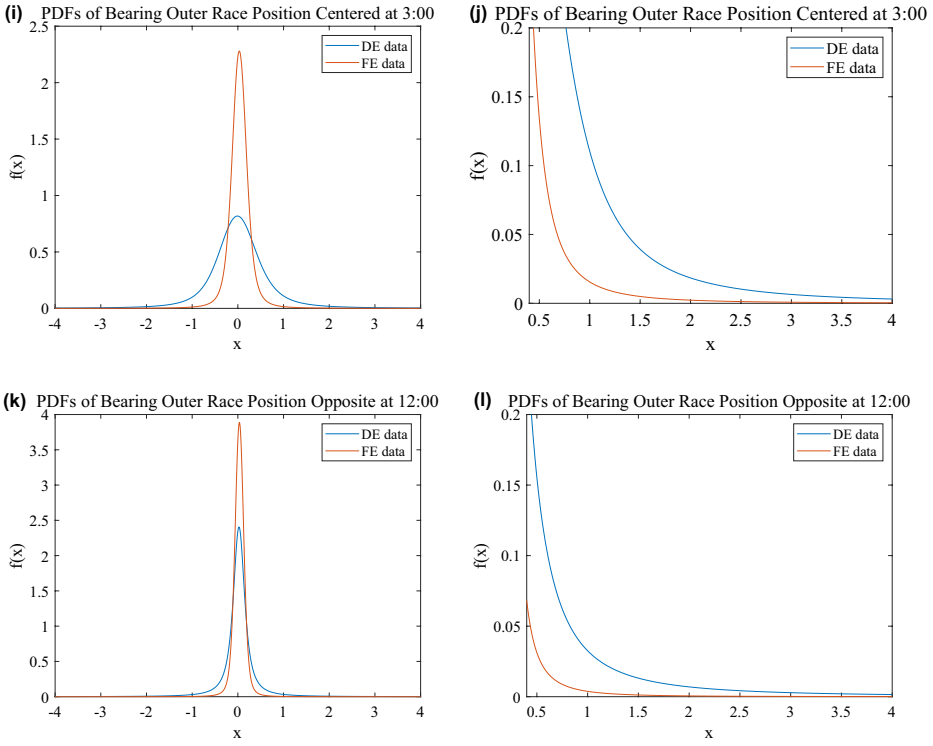

Figure 3. (continued)

$$FLOSSO = \int_{-\infty}^{+\infty} \delta[\eta - \varpi(t,\omega)]d\omega, \tag{4}$$

where $\int_{-\infty}^{+\infty} \delta[\eta - \omega_0(t,\omega)]d\omega$ is called the fractional low-order synchrosqueezing operator (FLOSSO) for $FLOSTFT_x(t,\omega)$, which uses instantaneous frequency (IF) to gather the FSTFT TF relevant coefficients with the same frequency, and the TF coefficients are readjusted to realize SSO of FSTFT time frequency representation indefinable energy into IF trajectory to improve its TF concentration. Similarly, according to the concept of SET in Ref.[9], we define a FSET as

$$FLOSET(t,\omega) = FLOSTFT_e(t,\omega) \cdot \delta[\omega - \varpi(t,\omega)], \tag{5}$$

where $FLOSTFT_e(t,\omega)$ is FSTFT in Eq. (2) considered an additional phase shift $e^{j\omega t}$ and a modulation operation, which can be written by

$$\begin{aligned} FLOSTFT_e(t,\omega) &= e^{j\omega t} FLOSTFT_x(t,\omega) \\ &= \frac{1}{2\pi} \int_{-\infty}^{+\infty} X^{<p>}(v) H(\omega - v) e^{-jvt} dv, \end{aligned} \tag{6}$$

where $X^{<p>}(v)$ and $H(\omega - v)$ are FLO Fourier transform(FLOFT) of the signal and window function, respectively. The Dirac function $\delta[\omega - \varpi(t,\omega)]$ in Eq. (5) is called the FLO synchroextracting operator (FLOSEO) for $FLOSTFT_x(t,\omega)$, and which can be written as

$$\delta[\omega - \varpi(t,\omega)] = \begin{cases} 1, & \omega = \varpi(t,\omega) \\ 0, & \omega \neq \varpi(t,\omega) \end{cases}. \tag{7}$$

Then Eq. (5) can be expressed as

$$FLOSET(t,\omega) = \begin{cases} FLOSTFT_e(t,\omega) & \omega = \varpi(t,\omega) \\ 0 & \omega \neq \varpi(t,\omega) \end{cases}. \tag{8}$$

FLOSEO in Eq. (5) can locate the energy peak value on IF trajectory based on the characteristics of maximum peak for some special points in FSTFT TF domain, so as to obtain a new TF coefficient.

When $FLOSTFT_e(t,\omega)$ in Eq. (6) is calculated partial derivative with respect to time, then

$$\begin{aligned}\partial_t[FLOSTFT_e(t,\omega)] &= \partial_t\left(\int_{-\infty}^{+\infty} x^{<p>}(\tau)h(\tau-t)e^{-j\omega(\tau-t)}d\tau\right)\backslash \\ &= \int_{-\infty}^{+\infty} x^{<p>}(\tau)\partial_t[h(\tau-t)]e^{-j\omega(\tau-t)}d\tau + \int_{-\infty}^{+\infty} x^{<p>}(\tau)h(\tau-t)\partial_t[e^{-j\omega(\tau-t)}]d\tau \\ &= -FLOSTFT_e^{h'}(t,\omega) + j\omega FLOSTFT_e(t,\omega),\end{aligned} \tag{9}$$

where $FLOSTFT_e^{h'}(t,\omega) = \int_{-\infty}^{+\infty} x^{<p>}(\tau)h'(\tau-t)e^{-j\omega(\tau-t)}d\tau$, and $h'(\tau-t)$ is the derivative of the window function $h(\tau-t)$ with respect to time, then

$$\frac{\partial_t[FLOSTFT_e(t,\omega)]}{jFLOSTFT_e(t,\omega)} = \frac{-FLOSTFT_e^{h'}(t,\omega)}{jFLOSTFT_e(t,\omega)} + \omega. \tag{10}$$

A mono-component non-stationary harmonic signal can be expressed as

$$s(t) = Ae^{j\varpi t}, \tag{11}$$

where A is invariant amplitude of the signal, then

$$s^{<p>}(t) = \frac{|A|^{p+1}}{(Ae^{j\varpi t})^*} = \frac{|A|^{p+1}}{A}e^{j\varpi t} = A^p e^{j\varpi t}. \tag{12}$$

Take the Fourier transform of the Eq. (11), then

$$S^p(v) = 2\pi A^p \delta(v-\varpi). \tag{13}$$

By substituting (13) into (6), the frequency domain representation of $FLOSTFT_e(t,\omega)$ can be written as

$$\begin{aligned}FLOSTFT_e(t,\omega) &= \frac{1}{2\pi}\int_{-\infty}^{+\infty} S^p(v)H(\omega-v)e^{jvt}dv \\ &= \frac{1}{2\pi}\int_{-\infty}^{+\infty} 2\pi A^p\delta(v-\varpi)H(\omega-v)e^{jvt}dv|_{v=\varpi} \\ &= A^p H(\omega-\varpi)e^{j\varpi t},\end{aligned} \tag{14}$$

where $H(\omega-v)$ is the Fourier transform of the window function $h(\tau-t)$. When Eq. (14) is calculated the partial derivative with respect to time, we can obtain

$$\begin{aligned}\partial_t[FLOSTFT_e(t,\omega)] &= \partial_t[A^p H(\omega-\varpi)e^{j\varpi t}] \\ &= A^p H(\omega-\omega_0)\partial_t[e^{j\varpi t}] \\ &= j\varpi FLOSTFT_e(t,\omega).\end{aligned} \tag{15}$$

And two-dimensional (2D) IF estimation can be expressed as

$$\varpi = \frac{\partial_t[FLOSTFT_e(t,\omega)]}{jFLOSTFT_e(t,\omega)}. \tag{16}$$

If we extend the single frequency point ϖ in Eq. (16) to all IF points (t,ω) in the FSTFT TF domain, then

$$\varpi(t,\omega) = \frac{\partial_t[FLOSTFT_e(t,\omega)]}{jFLOSTFT_e(t,\omega)}. \tag{17}$$

By substituting (17) into (3), FSST can be calculated. When $p=1$, FSTFT degenerates into STFT, FLOSSO degenerates into SSO, and FSST changes into SST. Hence, we hold the opinion that FSST is a generalized SST.

By combining Eqs. (10) and (17), then

$$\varpi(t,\omega) = \frac{-FLOSTFT_e^{h'}(t,\omega)}{jFLOSTFT_e(t,\omega)} + \omega. \tag{18}$$

When substituting (18) into (7), the calculation of FLOSEO can be expressed as

$$\delta[\omega - \varpi(t,\omega)] = \delta\left[\frac{FLOSTFT_e^{h'}(t,\omega)}{jFLOSTFT_e(t,\omega)}\right] = \begin{cases} 1, & \frac{FLOSTFT_e^{h'}(t,\omega)}{jFLOSTFT_e(t,\omega)} = 0 \\ 0, & \frac{FLOSTFT_e^{h'}(t,\omega)}{jFLOSTFT_e(t,\omega)} \neq 0 \end{cases}. \tag{19}$$

The Dirac function $\delta[\omega - \varpi(t,\omega)]$ can pinpoint the location of FSTFT TF coefficients which have the most energy on the IF trajectories. By substituting (19) into (5), FSET can be gotten. When $p = 1$, FSTFT degenerates into STFT, and FLOSEO and FSET degenerate into SEO and SET, respectively. Hence, FSET is a generalized SET.

Next we will discuss the TFR of the FSET and FSST methods. When Eq. (6) is calculated the integral with respect to frequency, we can obtain

$$\begin{aligned} \int_{-\infty}^{+\infty} FLOSTFT_e(t,\omega)d\omega &= \int_{-\infty}^{+\infty}\int_{-\infty}^{+\infty} x^{<p>}(\tau)h(\tau - t)e^{-j\omega(\tau - t)}d\tau d\omega \\ &= 2\pi x^{<p>}(t)h(0). \end{aligned} \tag{20}$$

Then, fractional p order moment of the original signal $x(t)$ can be written by

$$x^{<p>}(t) = \frac{1}{2\pi h(0)}\int_{-\infty}^{+\infty} FLOSTFT_e(t,\omega)d\omega. \tag{21}$$

According to Eq. (12), we can obtain

$$s^{<p>}(t) = A^p e^{j\varpi t} = A^{p-1}(Ae^{j\varpi t}) = A^{p-1}\cdot x(t). \tag{22}$$

Hence, the reconstructed original signal $x(t)$ can be expressed as

$$x(t) = \frac{A^{1-p}}{2\pi h(0)}\int_{-\infty}^{+\infty} FLOSTFT_e(t,\omega)d\omega. \tag{23}$$

When $FLOSTFT_e(t,\omega)$ in Eq. (23) are replaced by *FLOSST* in Eq. (3), we can obtain the reconstructed original signal $x(t)$ of the *FLOSST* method

$$x(t) = \frac{A^{1-p}}{2\pi h(0)}\int_{-\infty}^{+\infty} FLOSST(t,\eta)d\eta. \tag{24}$$

And by using *FLOSET* in Eq. (5) to substitute $FLOSTFT_e(t,\omega)$ in Eq. (23), the reconstructed original signal $x(t)$ employing the *FLOSET* method is gotten

$$x(t) = \frac{A^{1-p}}{2\pi h(0)}\int_{-\infty}^{+\infty} FLOSET(t,\omega)d\omega. \tag{25}$$

Inspired by the FSST, FSET and SSET methods, we replace $FLOSTFT_e(t,\omega)$ in Eq. (5)

with FSST in Eq. (3), then a robust FLO synchrosqueezing extracting transform (FSSET) method can be gotten

$$FLOSSET(t,\omega) = FLOSST(t,\omega)\cdot\delta[\omega - \varpi(t,\omega)]. \tag{26}$$

The method firstly synchrosqueezes the trajectory of IF in FSTFT the TF domain employing FLOSSO to improve the TF energy concentration, and then locates the energy peak based on SEO and changes the TF coefficient to improve the TF resolution. Because the advantages of FSST and FSET are combined, the improved FSSET method will have better performance advantages, which are embodied in more concentrated TFR and higher TF resolution. When $p = 1$, FSSET degenerates into SSET, hence, FSSET is a generalized SSET.

According to the reconstruction process of the FSET and FSST methods in Eq. (20)–(25), similarly, the TF reconstruction formula of the FSSET method can be written as

$$x(t) = \frac{A^{1-p}}{2\pi h(0)}\int_{-\infty}^{+\infty} FLOSSET(t,\omega)d\omega. \tag{27}$$

Application review

In this section, the proposed FSST, FSET and FSSET methods are applied to demonstrate their performance. The mixed signal contaminated by $v(t)$ (Gaussian or infinite variance process noise) is defined as

$$\begin{aligned} y(t) &= \sin\left[2\pi(50t + 20\sin t)\right] + \sin\left[2\pi t(2 + 9t)\right] + n(t) \\ &= x_1(t) + x_2(t) + n(t) = x(t) + n(t), \end{aligned} \tag{28}$$

where, $n(t)$ is infinite variance process noise, and when $\alpha = 2$, SNR can be used in Eq. (26). However, when $\alpha < 2$, which has no finite second moment and its variance is meaningless, then SNR is inapplicable. Hence, we can use the mixed signal noise ratio ($MSNR$) to replace SNR, and $MSNR$ can be expressed as

$$MSNR = 10\log_{10}(\sigma_x^2/\gamma), \tag{29}$$

where σ_x is variance of the signal $x(t)$, and γ is dispersion coefficient of α infinite variance process noise. The existing SST, SET and SSET methods and improved FSST, FSET and FSSET methods are compared to display TFR of the signal $x(t)$ in infinite variance process noise of the parameters $\alpha = 2$, $SNR = 8$ dB and $\alpha = 0.8$, $MSNR = 16$ dB, respectively, the results are given in Figs. 4 and 5.

In this simulation, we select $x_1(t)$ in Eq. (28) as the test signal. The mixed mean square error (MSE) is defined in Eq. (30), where, K is the number of Monte-Carlo experiment, $IF(t)$ is the real instantaneous frequency (IF), and $\hat{IF}(t)$ is the estimated IF based on ridges extraction and signal reconstruction employing the STFT, SST, SET, SSET, FSTFT, FSST, FSET or FSSET methods.

$$MSE = 10\log_{10}\left\{\frac{1}{K}\sum_{k=1}^{K}[\hat{IF}(t) - IF(t)]^2\right\}. \tag{30}$$

In order to further verify TFR performance of the existing and improved methods, let $K = 20$, $\alpha = 0.8$, $p = 0.2$, we conduct the following experiments with the analyzed signals $x_1(t)$ contaminated by infinite variance process noise at various $GSNR$(4 dB–22 dB). The Renyi Entropy, mixed MSEs of IF and $MSNR$—output comparisons are given in Fig. 6. And let $MSNR = 16$ dB, $p = 0.2$, $K = 20$, when α changes from 0.2 to 2, we apply the methods to compare in different α, the simulation results are shown in Fig. 7.

Remarks

Figure 4a,c,e,g are STFT, SST, SET and SSET methods TFR of the signal $x(t)$ in infinite variance process noise environment ($\alpha = 2$, $SNR = 8$ dB), respectively. And FSTFT, FSST, FSET and FSSET methods TFR are shown in Fig. 4b,d,f,h, respectively. It is shown that both the existing methods and the improved methods can give TF distribution of the signal $x(t)$ well. However, the STFT, SST, S ET and SSET methods fail under infinite variance process noise environment ($\alpha = 0.8$, $SNR = 16$ dB), as shown in Fig. 5a,c,e,g. But the improved FSTFT, FSST, FSET and FSSET methods in Fig. 5b,d,f,h, can still better demonstrate TFR of the signal $x(t)$. Hence, the proposed methods have wider applicability and better performance than the exiting methods, and they are robust.

Renyi Entropy, mixed MSEs of IF and $MSNR$—output comparisons of the STFT, SST, SET, SSET, FSTFT, FSST, FSET and FSSET methods are given in Fig. 6 in different $MSNR$ ($\alpha = 0.8, K = 20, p = 0.2$). The result show that improved FSTFT, FSST, FSET and FSSET methods exhibits relatively high quality in Gaussian ($\alpha = 2$) and α stable distributed noise ($\alpha < 2$) environments compared with existing methods. Among them, FSSET method has the best Renyi entropy in Fig. 6a, FSST method has the lowest mixed MSEs in Fig. 6b, and $MSNR$—output of FSTFT method is optimal in Fig. 6c.

Renyi entropy and mixed MSEs of IF comparisons of the STFT, SST, SET, SSET, FSTFT, FSST, FSET and FSSET methods are shown in Fig. 7 under different α ($MSNR = 16$ dB, $K = 20$, $p = 0.2$). By stabilizing the sensitivity of distributed noise parameters to these algorithms, the simulation of the difference between signals and the signal to noise ratio output measurement is restored. It can be seen that Renyi entropy of the FSSET method is least affected by the coefficient α, and the Renyi entropy of FSST and FSET methods is lower than that of the existing methods. FSST has the most consistent performance of ridges extraction and signal reconstruction.

Aiming at different $MSNR$ and infinite variance process noise parameters, the improved algorithms are superior to the existing ones in terms of algorithm sensitivity, signal reconstruction and $MSNR$ output measurement. FSST has the best reversibility and the highest quality of ridge estimation and signal reconstruction. Although FLOSECT has the best TF energy concentration, with the best Renyi Entropy value, it produces TF images with blurred and riven breaks because SECT removes many coefficients critical to characterizing m-D modes. Therefore, it is inferior to FSST algorithm in ridge estimation and signal reconstruction quality.

FSOSET method

Principle

According to definition of the GMLC signal model in Ref.[15], at every moment, FLO Gaussian modulated linear chirp model of the analyzed signal $x(t)$ can be defined as

$$\begin{aligned} \overline{x}(t) = \left[A(t)\cdot e^{j\varphi(t)}\right]^{<p>} &= \frac{A^{p+1}}{A\cdot e^{(t-t_0)^2/2T^2}e^{-j\varphi(t)}} \\ &= \overline{A}(t)\cdot e^{j\varphi(t)} = A^{p-1}\cdot x(t), \end{aligned} \tag{31}$$

where $A(t) = A\cdot e^{-(t-t_0)^2/2T^2}$, $\overline{A}(t) = A^p\cdot e^{-(t-t_0)^2/2T^2} = A^{p-1}\cdot A(t)$, and $\varphi(t) = a + bt + ct^2$. When $\overline{x}(t)$ is calculated the partial derivative with respect to time t, then

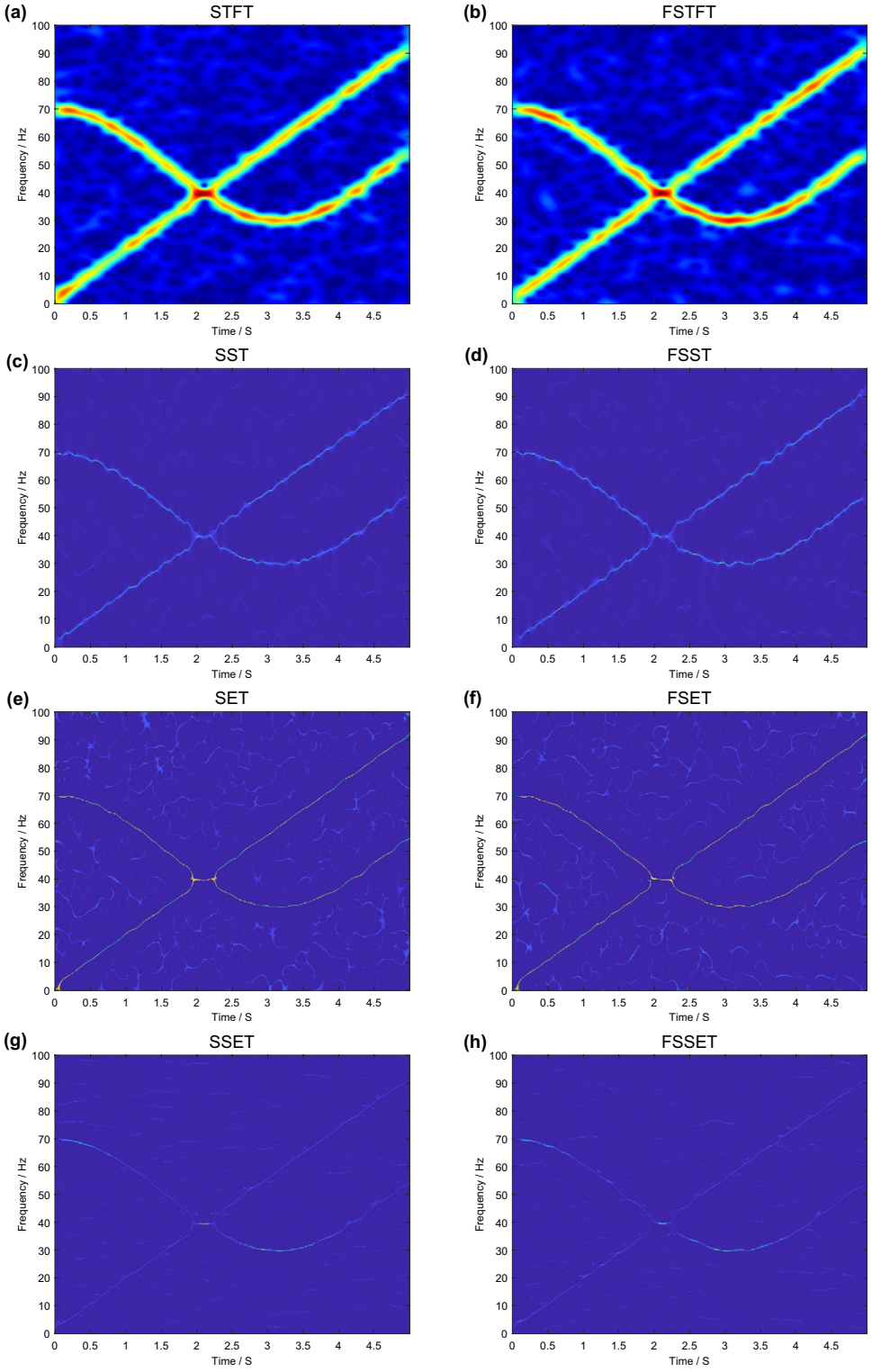

Figure 4. TFR of the signal $x(t)$ in infinite variance process noise environment ($\alpha = 2, SNR = 8$ dB). (**a**) STFT method; (**b**) FSTFT method; (**c**) SST method; (**d**) FSST method; (**e**) SET method; (**f**) FSET method; (**g**) SSET method; (**h**) FSSET method.

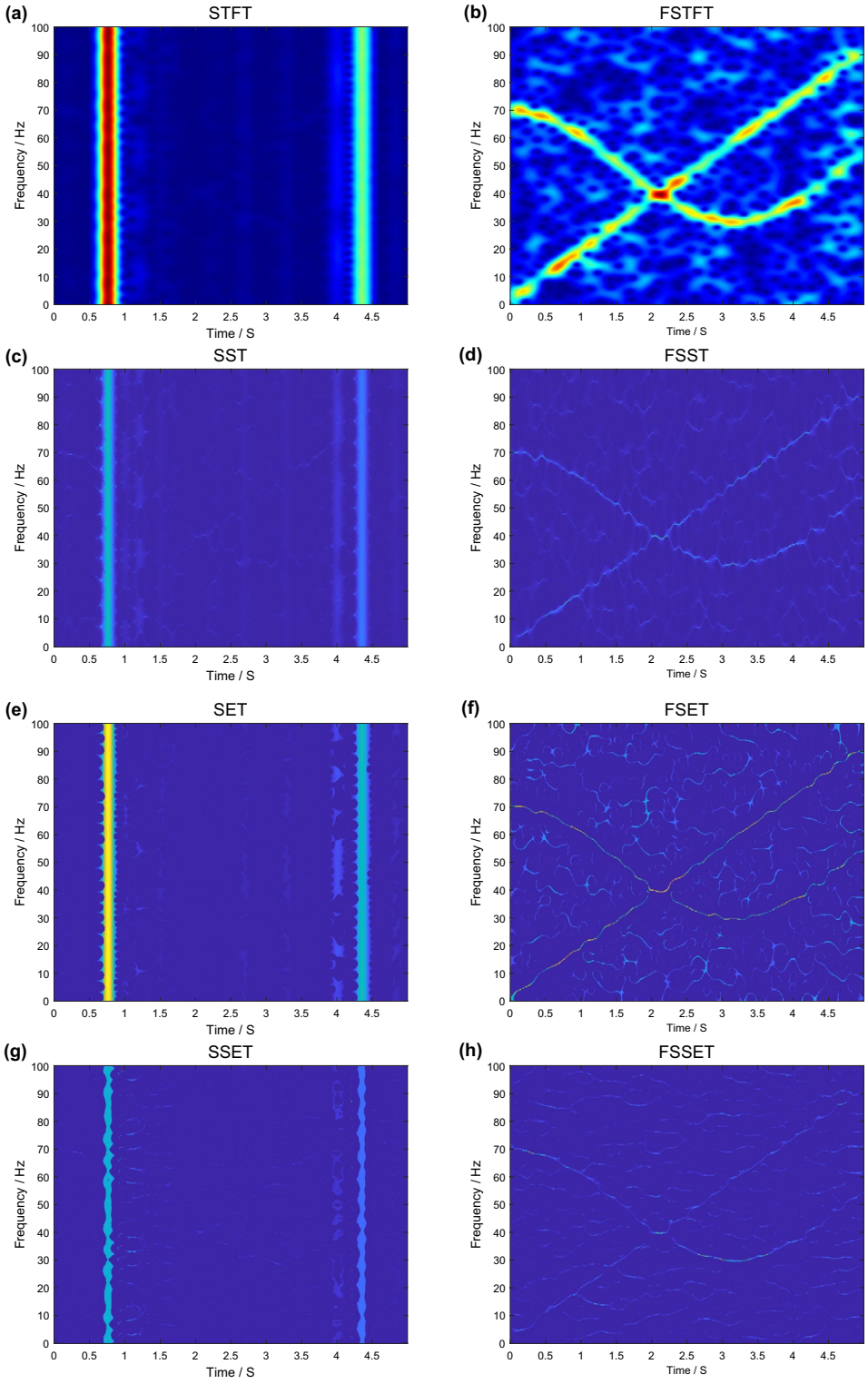

Figure 5. TFRs of the signal $x(t)$ in infinite variance process noise environment ($\alpha = 0.8$, $MSNR = 16$ dB). (**a**) STFT method; (**b**) FSTFT method; (**c**) SST method; (**d**) FSST method; (**e**) SET method; (**f**) FSET method; (**g**) SSET method; (**h**) FSSET method.

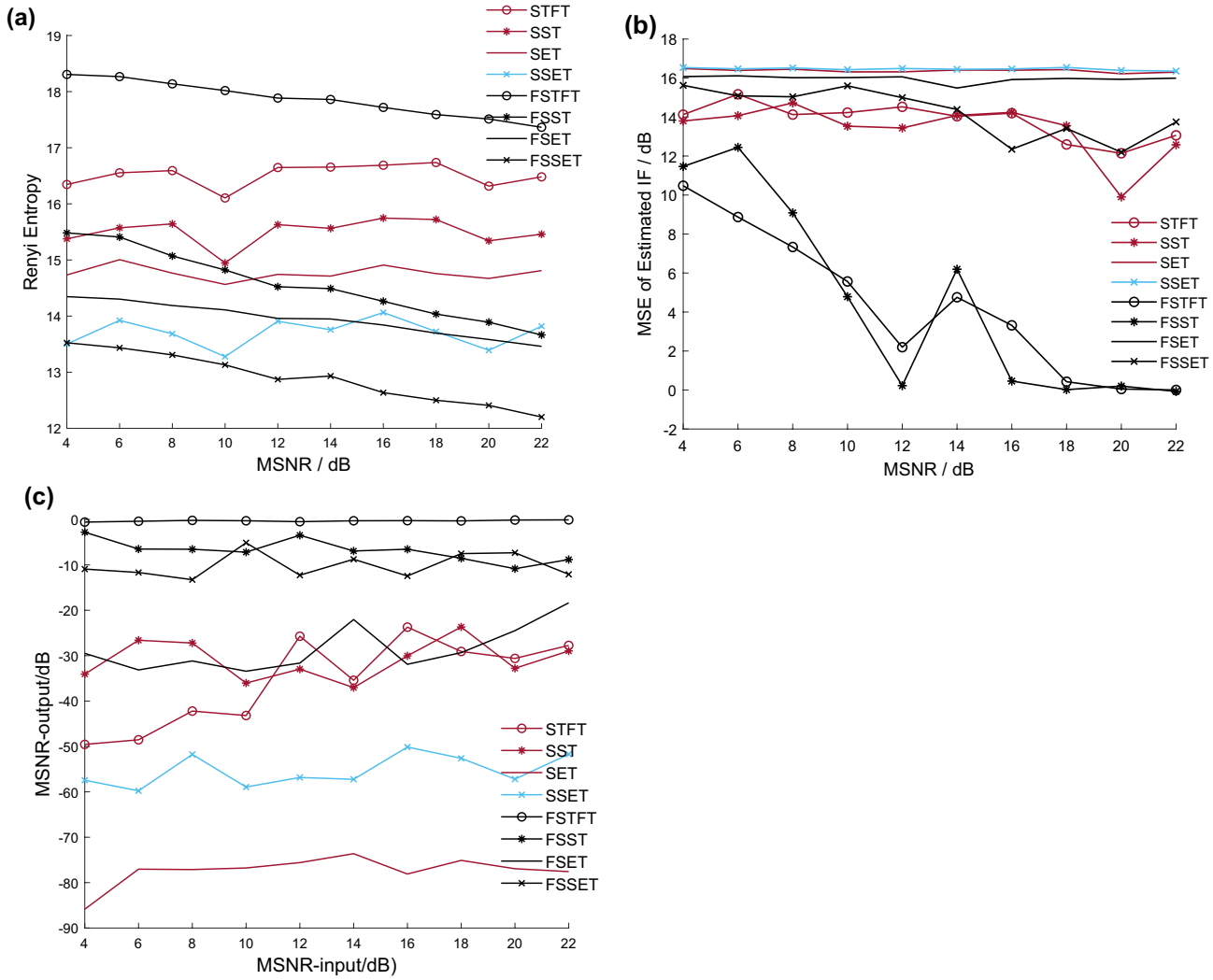

Figure 6. Renyi Entropy, mixed *MSE*s of IF and *MSNR*—output comparisons of the STFT, SST, SET, SSET, FSTFT, FSST, FSET and FSSET methods in different *MSNR* ($\alpha = 0.8$). (**a**) Renyi entropy; (**b**) mixed *MSE*s of IF; (**c**) *MSNR*—output).

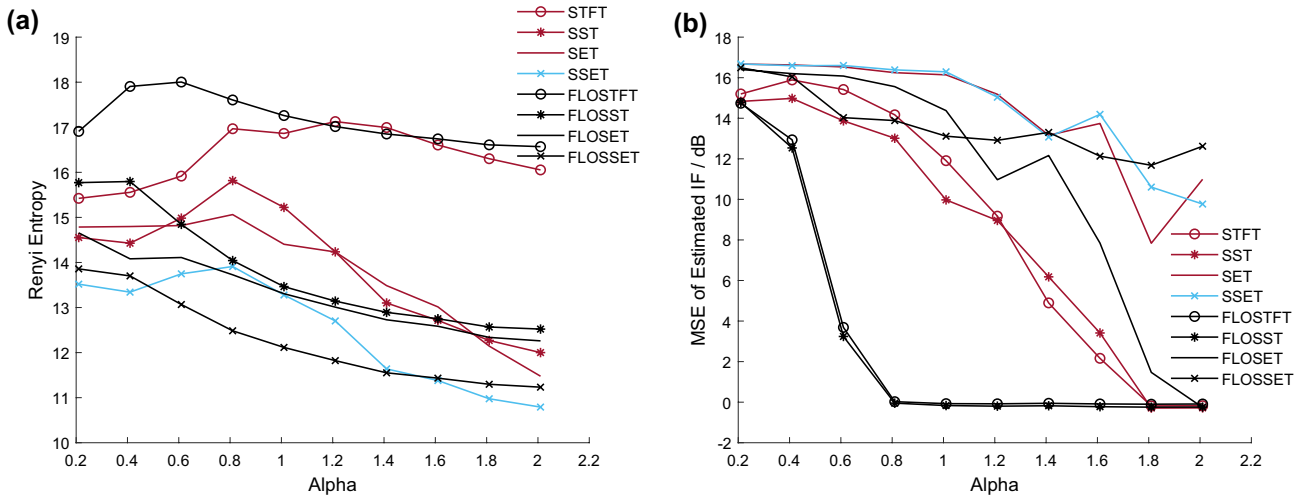

Figure 7. Renyi entropy and mixed *MSE*s of IF comparisons of the STFT, SST, SET, SSET, FSTFT, FSST, FSET and FSSET methods in different α(*MSNR* = 16 dB). (**a**) Renyi Entropy; (**b**) mixed *MSE*s of IF.

$$\begin{aligned}\partial_t[\overline{x}(t)] &= \partial_t[A^p \cdot e^{-(t-t_0)^2/2T^2} e^{j\varphi(t)}] \\ &= \partial_t[A^p \cdot e^{-(t-t_0)^2/2T^2}] \cdot e^{j\varphi(t)} + A^p \cdot e^{-(t-t_0)^2/2T^2} \partial_t[e^{j\varphi(t)}] \\ &= A^{p-1} \cdot x(t) \cdot \left[-\frac{t-t_0}{T^2} + j(b+2ct) \right] \\ &= \overline{x}(t) \cdot [p+qt],\end{aligned} \tag{32}$$

where $p = \frac{t_0}{T^2} + jb, q = -\frac{t}{T^2} + j2c$, and $p + qt$ can be called as the instantaneous complex frequency, when we extract its imaginary part, then

$$\begin{aligned}\mathrm{IM}(p+qt) &= \mathrm{IM}\left[\left(\frac{t_0}{T^2} + jb\right) + \left(-\frac{t}{T^2} + j2c\right)\right] t \\ &= b + 2ct = \partial(\varphi(t)) = \varphi'(t).\end{aligned} \tag{33}$$

Because $FLOSTFT'_x(t,\omega)$ in Eq. (6) is $FLOSTFT_x(t,\omega)$ considered an additional phase shift $e^{j\omega t}$, and its partial derivative with respect to time t can be expressed as

$$\begin{aligned}\partial_t[FLOSTFT_e(t,\omega)] &= \partial_t\left(\int_{-\infty}^{+\infty} x^{<p>}(\tau) h(\tau - t) e^{-j\omega(\tau - t)} d\tau\right) \\ &= \int_{-\infty}^{+\infty} x^{<p>}(\tau) \partial_t[h(\tau - t)] e^{-j\omega\tau} d\tau \\ &= \int_{-\infty}^{+\infty} \partial_t\left(x^{<p>}(\tau + t)\right) h(\tau) e^{-j\omega\tau} d\tau.\end{aligned} \tag{34}$$

According to Eq. (32), we can obtain $\partial_t[x^{<p>}(\tau + t)] = \overline{x}(\tau + t) \cdot [p + q(\tau + t)]$, then

$$\begin{aligned}\partial_t[FLOSTFT_e(t,\omega)] &= \int_{-\infty}^{+\infty} \left(\overline{x}(\tau + t) \cdot (p + q(t + \tau))\right) h(\tau) e^{-j\omega\tau} d\tau \\ &= \int_{-\infty}^{+\infty} \left(\overline{x}(\tau + t) \cdot (p + qt)\right) h(\tau) e^{-j\omega\tau} d\tau + \int_{-\infty}^{+\infty} \overline{x}(\tau + t) \cdot q\tau h(\tau) e^{-j\omega\tau} d\tau \\ &= (p + qt) FLOSTFT_e(t,\omega) + q \cdot FLOSTFT_e^{th}(t,\omega),\end{aligned} \tag{35}$$

where $FLOSTFT_e^{th}(t,\omega)$ is the FSTFT result employing the analytic window function $\tau h(\tau)$. By combining Eqs. (9) and (35), we get

$$-FLOSTFT_e^{h'}(t,\omega) + j\omega FLOSTFT_e(t,\omega) = (p + qt) FLOSTFT_e(t,\omega) + q \cdot FLOSTFT_e^{th}(t,\omega). \tag{36}$$

Then

$$FLOSTFT_e^{h'}(t,\omega) = (j\omega - p - qt) FLOSTFT_e(t,\omega) - q \cdot FLOSTFT_e^{th} t,\omega). \tag{37}$$

The derivative of both sides of Eq. (37) with respect to time t is obtained

$$FLOSTFT_e^{h''}(t,\omega) = (j\omega - p - qt) FLOSTFT_e^{h'}(t,\omega) - q \cdot FLOSTFT_e^{th'}(t,\omega), \tag{38}$$

where $FLOSTFT_e^{h''}(t,\omega)$ represents FSTFT result using the analytic window function $\frac{d^2h(t)}{dt^2}$, and $FLOSTFT_e^{th}(t,\omega)$ is a FSTFT result with the analytic window function $\tau(\partial_t h'(\tau))$. By solving Eqs. (37) and (38), we can obtain

$$p + qt = \frac{FLOSTFT_e^{h''}(t,\omega) \cdot FLOSTFT_e^{th}(t,\omega) - FLOSTFT_e^{h'}(t,\omega) \cdot FLOSTFT_e^{th'}(t,\omega)}{FLOSTFT_e(t,\omega) \cdot FLOSTFT_e^{th'}(t,\omega) - FLOSTFT_e^{th}(t,\omega) \cdot FLOSTFT_e^{h'}(t,\omega)} - j\omega. \tag{39}$$

By substituting Eq. (39) into Eq. (33), then FLO second-order synchroextracting operator (FLOSOSEO) can be written by Eq. (40), which can realize the extraction of second order IF.

$$\begin{aligned}\varpi_2(t,\omega) &= \mathrm{IM}(p + qt) \\ &= \mathrm{IM}[\frac{FLOSTFT_e^{h''}(t,\omega) \cdot FLOSTFT_e^{th}(t,\omega) - FLOSTFT_e^{h'}(t,\omega) \cdot FLOSTFT_e^{th'}(t,\omega)}{FLOSTFT_e(t,\omega) \cdot FLOSTFT_e^{th'}(t,\omega) - FLOSTFT_e^{th}(t,\omega) \cdot FLOSTFT_e^{h'}(t,\omega)}] - \omega.\end{aligned} \tag{40}$$

By employing $\varpi_2(t,\omega)$ to replace $\varpi(t,\omega)$ in Eq. (5), FLO second-order synchroextracting transform (FSOSET) can be defined as

$$FLOSOSET(t,\omega) = FLOSTFT_e(t,\omega) \cdot \delta[\omega - \varpi_2(t,\omega)]. \tag{41}$$

When $p = 1$, FSTFT degenerates into STFT, and FSOSET degenerate into $SET2$. Therefore, we can draw a conclusion that FSOSET is a generalized $SET2$. The reconstructed original signal $x(t)$ of the $FLOSOSET$ method can be written as

$$x(t) = \frac{A^{1-p}}{2\pi h(0)} \int_{-\infty}^{+\infty} FLOSOSET(t,\omega)d\omega. \tag{42}$$

Application review

In this section, we select $x(t)$ as the test signal. Firstly, we will discuss the performances of the $FLOSOSET$ and $SET2$ methods. The existing $SET2$ method and the improved FSOSET ($p = 0.2$) method to demonstrate TFR of the signal $x(t)$ in Eq. (28) in infinite variance process noise environment ($\alpha = 2$, $SNR = 8$ dB) and infinite variance process noise environment ($\alpha = 0.8$, $MSNR = 16$ dB), the results are given in Figs. 8 and 9, respectively.

In order to further verify TFR performance of the existing SOSET and improved FSOSET methods, let $K = 10$, $\alpha = 0.8$, $p = 0.2$, we conduct the following experiments with the analyzed signals $x_1(t)$ contaminated by infinite variance process noise at various $GSNR$ (4–22 dB). The Renyi Entropy, mixed MSEs of IF and $MSNR$—output comparisons are given in Fig. 10. And let $MSNR = 16$ dB, $p = 0.2$, $K = 10$, when α changes from 0.2 to 2, we apply the methods to compare in different α, the simulation results are shown in Fig. 11.

Remarks

Figure 9a,b are SOSET and FSOSET methods TFR of the signal $x(t)$ under infinite variance process noise environment ($\alpha = 2$, $SNR = 8$ dB), respectively. The TF distribution of SOSET and FSOSET methods are shown in Fig. 10a,b, respectively. It can be seen that both methods have good TF performance in infinite variance process

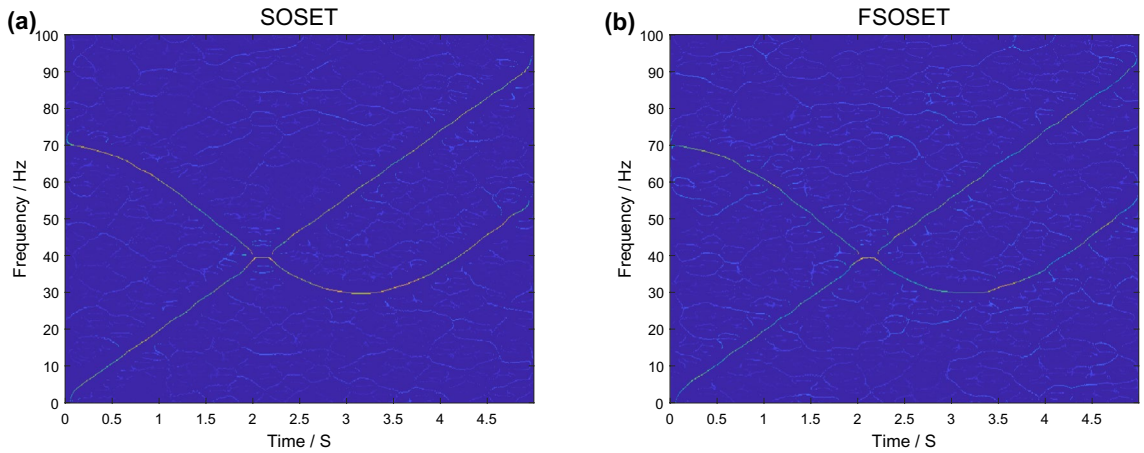

Figure 8. TFR of the signal $x(t)$ in infinite variance process noise environment ($\alpha = 2$, $SNR = 8$ dB). (**a**) SOSET method; (**b**) FSOSET method.

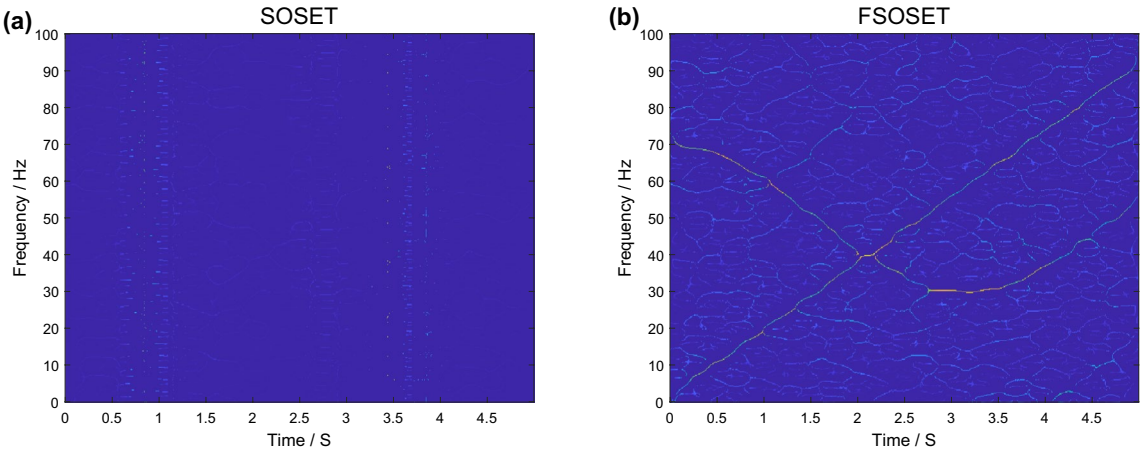

Figure 9. TFR of the signal $x(t)$ in infinite variance process noise environment ($\alpha = 0.8$, $MSNR = 16$ dB). (**a**) SOSET method; (**b**) FSOSET method.

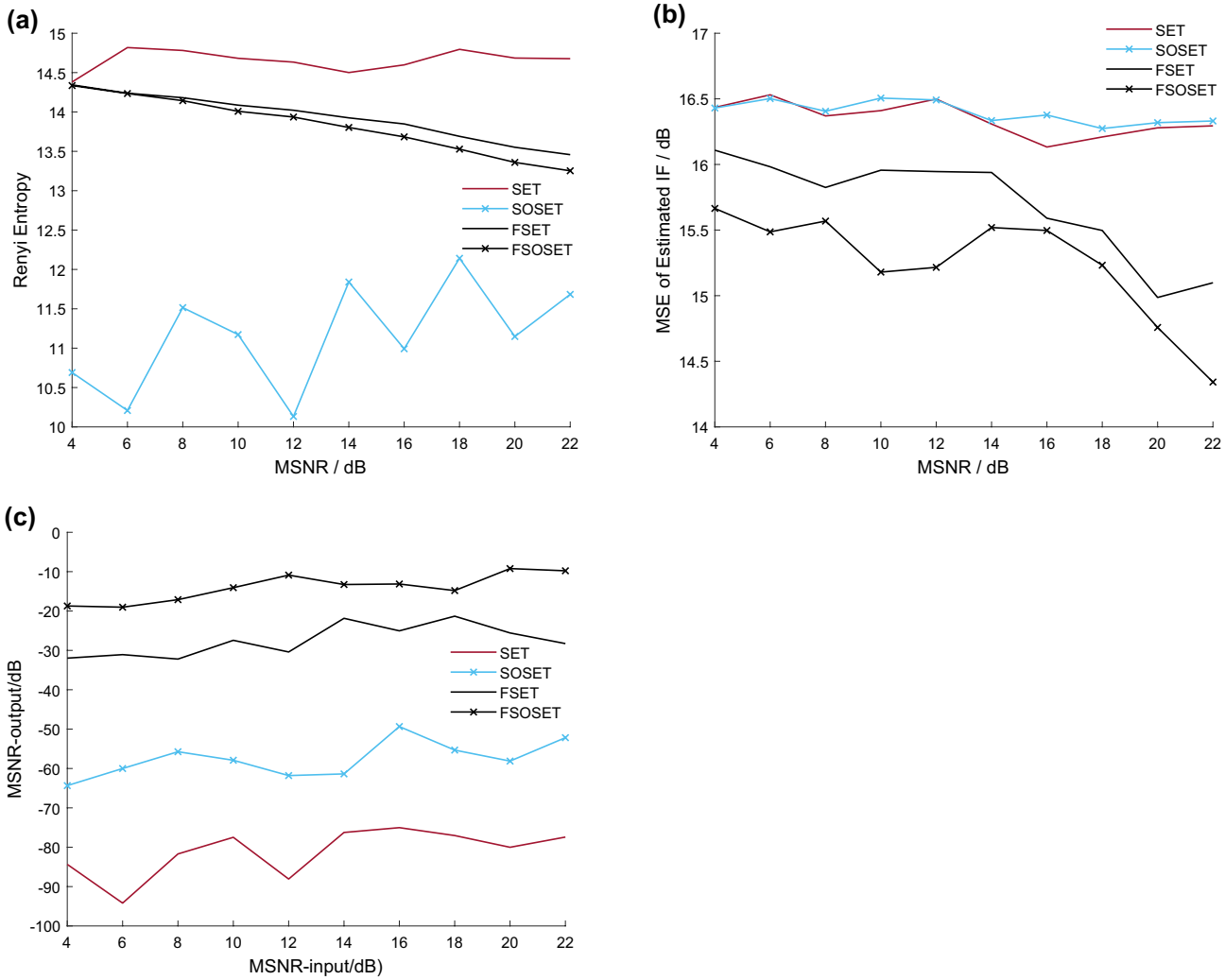

Figure 10. Renyi Entropy, mixed *MSE*s of IF and *MSNR*—output comparisons of the SET, FSET, SOSET and FSOSET methods in different *MSNR* ($\alpha = 0.8$). (**a**) Renyi Entropy; (**b**) Mixed *MSE*s of IF; (**c**) *MSNR*—output.

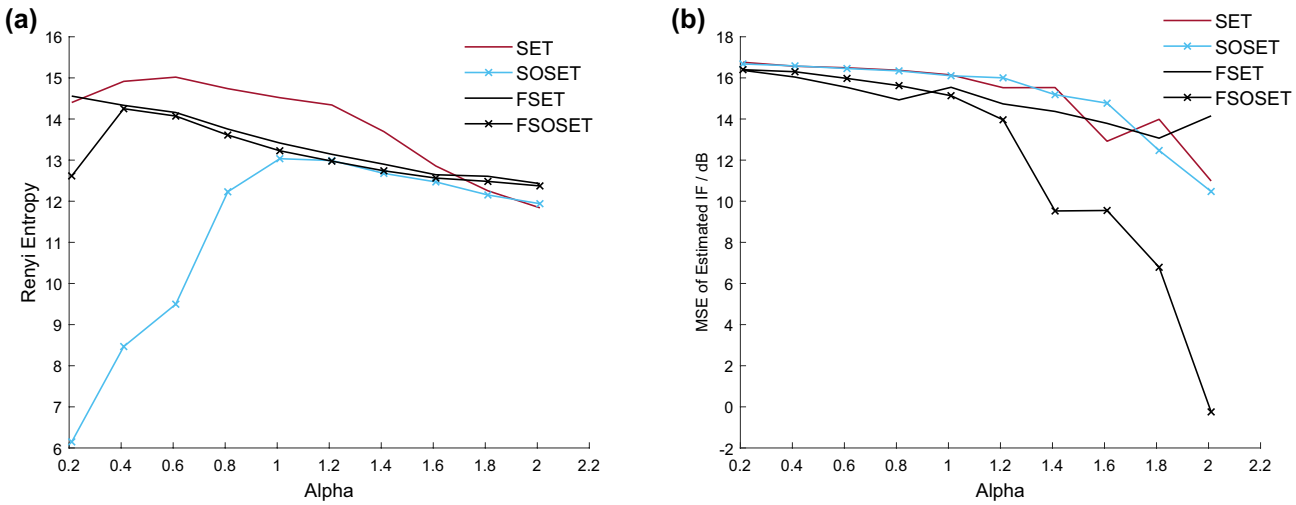

Figure 11. Renyi entropy and mixed *MSE*s of IF comparisons of the SET, FSET, SOSET and FSOSET methods in different α (*MSNR* = 16 dB). (**a**) Renyi entropy; (**b**) mixed *MSE*s of IF.

noise environment. However, the SOSET method fail under infinite variance process noise environment ($\alpha = 0.8$, $SNR = 16$ dB), but the improved FSOSET method still works well. Hence, the FSOSET method have wider applicability and better performance than the SOSET method, and they are robust.

Combined with ridge extraction techniques, Fig. 10 show that Renyi Entropy, mixed *MSE*s of IF and *MSNR* —output comparisons of the SET, FSET, SOSET and FSOSET methods in different *MSNR* ($\alpha = 0.8$), respectively. We can see that FSOSET method has the smallest reconstruction error of transient signal and the strongest noise suppression ability. However, its Renyi Entropy is inferior to that of SOSET method. The proposed FSOSET method shows the advantages of TF reconstruction and the ability of noise suppression in different α ($MSNR = 16$ dB), as show in Fig. 11, in particular, when $\alpha > 1$, its advantages are more obvious.

FMSST method

Principle

According to FSST formula in Eq. (3) and the MSST method, we also make iterative improvements on it, so it can be called FLO multi-synchrosqueezing transform (FMSST), the first iteration of FMSST of the analyzed signal $x(t)$ can be written by

$$FLOMSST_1(t,\eta) = \int_{-\infty}^{+\infty} FLOSST(t,\eta)\cdot\delta[\eta - \varpi(t,\omega)]d\omega. \tag{43}$$

By substituting Eq. (3) into Eq. (43), then

$$\begin{aligned} FLOMSST_1(t,\eta) &= \int_{-\infty}^{+\infty} FLOSST(t,\nu)\cdot\delta[\eta - \varpi(t,\nu)]d\nu \\ &= \int_{-\infty}^{+\infty} FLOSTFT_e(t,\omega)\delta[\eta - \varpi(t,\varpi(t,\omega))]d\omega. \end{aligned} \tag{44}$$

The FMSST method uses IF estimation function $\varpi(t,\varpi(t,\omega))$ to redistribute and centralize the fuzzy energy in the FSTFT TF domain, which is the first iteration of the IF estimation function $\varpi(t,\omega)$ employing FSST. If we carry out the second iteration, then

$$\begin{aligned} FLOMSST_2(t,\eta) &= \int_{-\infty}^{+\infty} FLOMSST_1(t,\nu)\cdot\delta[\eta - \varpi(t,\nu)]d\nu \\ &= \int_{-\infty}^{+\infty} FLOSTFT_e(t,\omega)\delta[\eta - \varpi(t,\varpi(t,\varpi(t,\omega)))]d\omega. \end{aligned} \tag{45}$$

When we continue the iterative calculation, then the N times iteration FMSST calculation of the analyzed signal $x(t)$ can be written as

$$\begin{aligned} FLOMSST_N(t,\eta) &= \int_{-\infty}^{+\infty} FLOMSST_{N-1}(t,\nu)\cdot\delta[\eta - \varpi(t,\nu)]d\nu \\ &= \int_{-\infty}^{+\infty} FLOSTFT_e(t,\omega)\cdot\delta[\eta - \varpi_N(t,\omega)]d\omega, \end{aligned} \tag{46}$$

where $\varpi_N(t,\omega)$ denotes IF estimation function of the N times iteration, and $\varpi_1(t,\omega) = \varpi(t,\varpi(t,\omega))$,

$$\varpi_2(t,\omega) = \varpi(t,\varpi(t,\varpi(t,\omega))),\ \varpi_3(t,\omega) = \varpi(t,\varpi(t,\varpi(t,\varpi(t,\omega)))),\ldots,\varpi_N(t,\omega).$$

Next, we will discuss the calculation of IF estimation function $\varpi_N(t,\omega)$. According to the Taylor expansion, $\varphi(t)$ in Eq. (31) can be expanded at the time point t, then

$$\overline{x}(\tau) = x^{<p>}(\tau) = \overline{A}(t)\cdot e^{j[\varphi(t)+\varphi'(t)(\tau-t)+0.5\varphi''(t)(\tau-t)^2]}. \tag{47}$$

According to Eq. (6), we can obtain

$$\begin{aligned} FLOSTFT_e(t,\omega) &= \int_{-\infty}^{+\infty} x^{<p>}(\tau)h(\tau-t)e^{-j\omega(\tau-t)}d\tau \\ &= \int_{-\infty}^{+\infty} \overline{A}(t)\cdot e^{j[\varphi(t)+\varphi'(t)(\tau-t)+0.5\varphi''(t)(\tau-t)^2]}h(\tau-t)e^{-j\omega(\tau-t)}d\tau. \end{aligned} \tag{48}$$

A Gaussian window function can be written by

$$h(t) = (\pi\sigma^2)^{-\frac{1}{4}} \cdot e^{-\frac{t^2}{2\sigma^2}}. \tag{49}$$

By substituting $h(\tau - t)$ into Eq. (48), then

$$\begin{aligned} FLOSTFT_e(t,\omega) &= \int_{-\infty}^{+\infty} (\pi\sigma^2)^{-\frac{1}{4}} \cdot \overline{A}(t) \cdot e^{j[\varphi(t)+\varphi'(t)(\tau-t)+0.5\varphi''(t)(\tau-t)^2]} \cdot e^{-\frac{(\tau-t)^2}{2\sigma^2}} \cdot e^{-j\omega(\tau-t)} d\tau \\ &= (\pi\sigma^2)^{-\frac{1}{4}} \cdot \overline{A}(t) e^{j\varphi(t)} \cdot \frac{1}{\sqrt{\frac{1}{\sigma^2} - j\varphi''(t)}} \cdot e^{-\frac{[\omega-\varphi'(t)]^2}{\frac{2}{\sigma^2}-j2\varphi''(t)}}. \end{aligned} \tag{50}$$

By substituting Eq. (50) into Eq. (16), then IF estimation of the analyzed signal $x(t)$ can be expressed as

$$\varpi(t,\omega) = \varphi'(t) + \frac{\varphi''(t)^2}{(1/\sigma)^2 + \varphi''(t)^2}[\omega - \varphi'(t)] - j\frac{\varphi''(t)}{(1/\sigma)^2 + \varphi''(t)^2}[\omega - \varphi'(t)]. \tag{51}$$

Because the result of Eq. (51) is a complex number, we use the real part of Eq. (51) for the actual calculation, in that way

$$\varpi(t,\omega) \triangleq \mathrm{IM}(\varpi(t,\omega)) = \varphi'(t) + \frac{\varphi''(t)^2}{(1/\sigma)^2 + \varphi''(t)^2}[\omega - \varphi'(t)]. \tag{52}$$

When $N = 1$, the corresponding IF estimation function of the first time iteration $\varpi_1(t,\omega) = \varpi(t, \varpi(t,\omega))$ can be written by

$$\begin{aligned} \varpi_1(t,\omega) = \varpi(t,\varpi(t,\omega)) &= \varphi'(t) + \frac{\varphi''(t)^2}{(1/\sigma)^2 + \varphi''(t)^2}[\varpi(t,\omega) - \varphi'(t)] \\ &= \varphi'(t) + [\frac{\varphi''(t)^2}{(1/\sigma)^2 + \varphi''(t)^2}]^2[\omega - \varphi'(t)]. \end{aligned} \tag{53}$$

And

$$\begin{aligned} \varpi_2(t,\omega) = \varpi(t,\varpi(t,\varpi(t,\omega))) &= \varphi'(t) + \frac{\varphi''(t)^2}{(1/\sigma)^2 + \varphi''(t)^2}[\varpi(t,\varpi(t,\omega)) - \varphi'(t)] \\ &= \varphi'(t) + \left[\frac{\varphi''(t)^2}{(1/\sigma)^2 + \varphi''(t)^2}\right]^3 [\omega - \varphi'(t)]. \end{aligned} \tag{54}$$

Hence, IF estimation function of the N times iteration $\varpi_N(t,\omega)$ can be written as

$$\varpi_N(t,\omega) = \varphi'(t) + \left[\frac{\varphi''(t)^2}{(1/\sigma)^2 + \varphi''(t)^2}\right]^{N+1} [\omega - \varphi'(t)]. \tag{55}$$

By substituting Eq. (55) into Eq. (46), we can get the N times iteration FMSST calculation of the analyzed signal $x(t)$.

Compared with RM method, the FMSST method only redistributes the TFR in the frequency direction, so no data information should be lost theoretically, and which can reconstruct the original signal $x(t)$ more perfectly, the reconstruction process is as follows:

$FLOMSST_N(t,\eta)$ in Eq. (46) takes the integral with respect to frequency η, then

$$\begin{aligned}\int_{-\infty}^{+\infty} FLOMSST_N(t,\eta)d\eta &= \int_{-\infty}^{+\infty}\int_{-\infty}^{+\infty} FLOMSST_{N-1}(t,v)\cdot\delta[\eta-\varpi(t,v)]dvd\eta\\ &= \int_{-\infty}^{+\infty} FLOMSST_{N-1}(t,v)dv\\ &\vdots\\ &= \int_{-\infty}^{+\infty} FLOMSST_1(t,v)dv\\ &= 2\pi\int_{-\infty}^{+\infty} x^{<p>}(\tau)h(\tau-t)\delta(\tau-t)d\tau\\ &= 2\pi h(0)A^{p-1}\cdot x(\tau).\end{aligned} \tag{56}$$

According to Eq. (56), the reconstructed original signal $x(t)$ employing the FMSST method can be expressed as

$$x(t) = \frac{A^{1-p}}{2\pi h(0)}\int_{-\infty}^{+\infty} FLOMSST_N(t,\omega)d\omega. \tag{57}$$

Application review

In this section, $y(t)$ in Eq. (28) is used as the test signal. Firstly, the performances of the Nth iteration MSST and FMSST methods are studied. The existing methods and the improved methods are applied to demonstrate TFR of the signal $x(t)$ under infinite variance process noise environment ($\alpha = 2, SNR = 8$ dB) and infinite variance process noise environment ($\alpha = 0.8, MSNR = 16$ dB), the TF results are shown in Figs. 12 and 13, respectively.

In order to further verify TFR performance of the existing Nth iteration MSST and improved FMSST methods, we let $K = 10, \alpha = 0.8, p = 0.2$, and have done the following experiments with the analyzed signals $x_1(t)$ contaminated by infinite variance process noise under different *GSNR* (4 dB–22 dB), the Renyi Entropy, mixed *MSE*s of IFs and *MSNR*—output comparisons are shown in Fig. 14. Moreover, we let $MSNR = 16dB$, $p = 0.2$, $K = 10$, and repeat the above simulation experiment for the Nth iteration MSST and FMSST methods under different α (0.2–2), the simulation results are given in Fig. 15.

Remarks

Figure 11a,c,e are the 1st, 2nd and 8th order MSST methods TFR of the signal $x(t)$ under infinite variance process noise conditions ($\alpha = 2, SNR = 8$ dB), respectively. And the 1st, 2nd and 8th order FMSST methods TF distributions of the signal $x(t)$ are shown in Fig. 11b,d,f, respectively. It can be seen from Fig. 10 that the methods can give their TFRs very well in infinite variance process noise environment. However, the 1st, 2nd and 8th order MSST methods fail in infinite variance process noise conditions ($\alpha = 0.8, SNR = 16$ dB), as shown in Fig. 12a,c,e, but the improved Nth iteration FMSST methods in Fig. 12b,d,f still have good results.

Figure 13a–c are Renyi Entropy, mixed *MSE*s of IF and *MSNR*—output comparisons of the Nth iteration MSST and FMSST methods employing the ridge extraction techniques under infinite variance process noise ($\alpha = 0.8$) and different *MSNR* (4–22 dB), respectively. It can be seen from Fig. 13 that the improved Nth iteration FMSST methods are better than the corresponding Nth iteration MSST methods in Renyi Entropy, mixed of IF and output. The 8th iteration FMSST method has the smallest Renyi Entropy, the 2th iteration FMSST method has the fastest convergence of IF reconstruction error of transient signal, and their *MSNR*—output is almost equivalent. Hence, the improved iteration FMSST methods have stronger noise suppression ability than the exiting methods.

Figure 14 shows Renyi Entropy and mixed *MSE*s of IF of the Nth iteration MSST and FMSST methods employing the ridge extraction techniques under infinite variance process noise ($MSNR = 16$ dB) and different α (0.2–2), respectively. It can be seen that the robust post-processing TFR methods have obvious advantages of TF reconstruction and the ability of noise suppression when $\alpha < 1.6$, and when $\alpha > 1.6$, they have almost the same Mixed *MSE*s of IF. Therefore, the Nth iteration FMSST method is more suitable for different complex environments and has better TF energy aggregation than the MSST method.

Application simulations

In this section, the test signal uses the bearing outer ring DE fault position relative to the center of the load zone at 6:00, the signal length is 0.2 s, then $N = 2400$. The conventional SET, SSET, SOSET and Nth iteration MSST methods, the improved FSET, FSSET, FSOSET and Nth iteration FMSST methods have been used to extract the fault feature of the DE fault signals polluted by infinite variance process noise. The results are shown in Figs. 16 and 17.

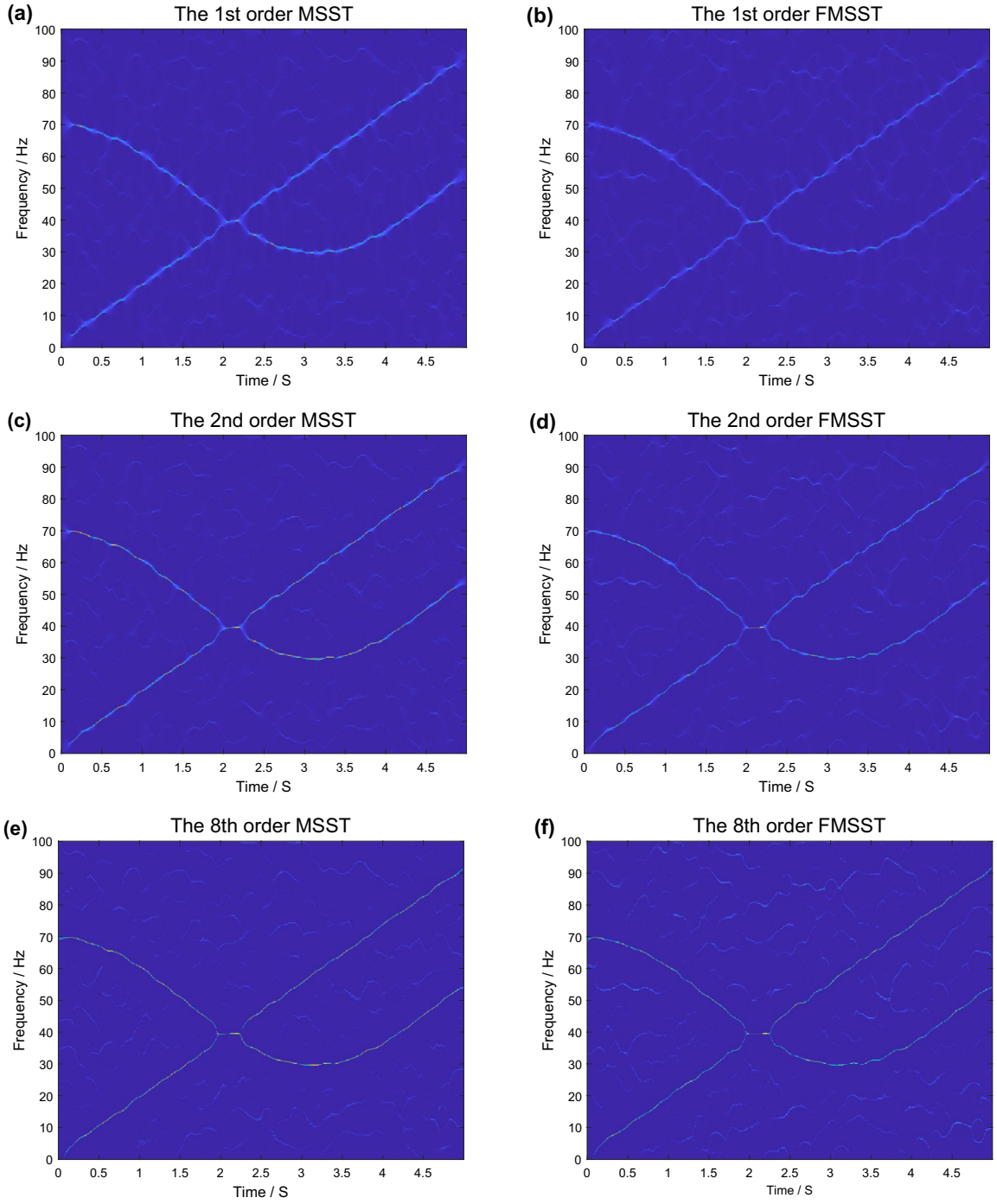

Figure 12. TFR of the signal $x(t)$ in infinite variance process noise environment ($\alpha = 0.8, SNR = 8$ dB). (**a**) The 1st order MSST method. (**b**) The 1st order FMSST method. (**c**) The 2nd order MSST method. (**d**) The 2nd order FMSST method. (**e**) The 8th order MSST method. (**f**) The 8th order FMSST method.

SET and FLOSET ($p = 0.8$) of the outer race DE fault position relative to load zone centered at 6:00 data polluted by infinite variance process noise($\alpha = 2, SNR = 5$ dB) are given in Fig. 16a,b, respectively. Figure 16c,d are the SSET and FSSET, respectively. SOSET and FSOSET TF distributions are in Fig. 16e,f. Figure 16g,h respectively are the 1st iteration MSST and FMSST method. The 8th iteration MSST and FMSST method are shown in Fig. 16i,j. The results show that both the proposed robust synchronous compression and synchronous extraction transform TFR method and the traditional method can extract and diagnose the signal polluted by α stable distributed noise ($\alpha = 2$), and the transient harmonic vibration frequency of the DE fault signal of the bearing outer ring changes regularly. The fault vibration frequency ranges from 0 to 4000 Hz and is concentrated in the vicinity of 600 Hz, 2800 Hz, and 3500 Hz. The time between the vibration pulses A, B, C, D, E, and F is about 33 ms, so the characteristic frequency can be calculated to be about 30Hz.

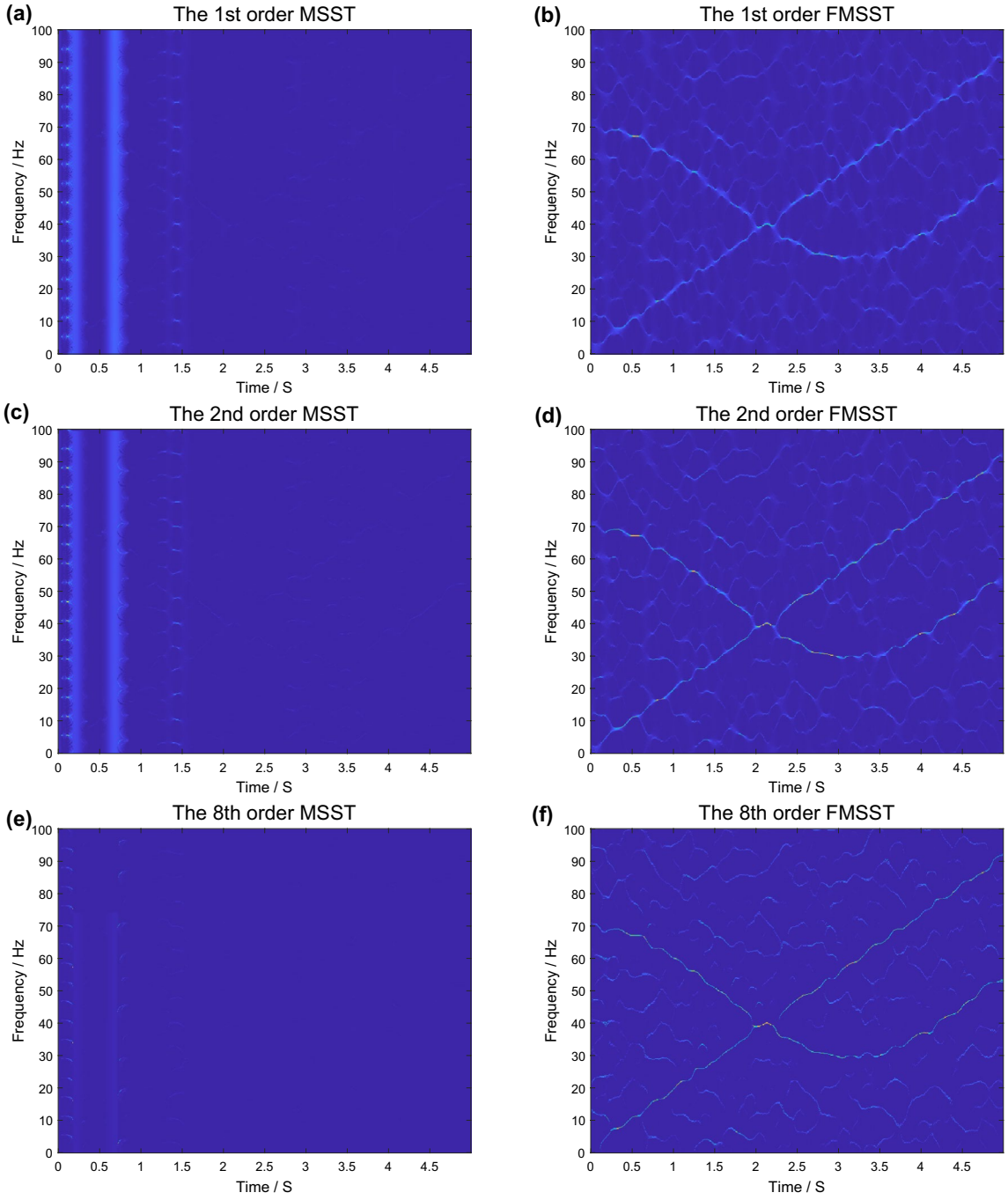

Figure 13. TFRs of the signal $x(t)$ under infinite variance process noise environment ($\alpha = 0.8$, $MSNR = 16$ dB). (**a**) The 1st order MSST method. (**b**) The 1st order FMSST method. (**c**) The 2nd order MSST method. (**d**) The 2nd order FMSST method. (**e**) The 8th order MSST method. (**f**) The 8th order FMSST method).

Figure 17 shows from a to j: SET, FSET, SSET FSSET, SOSET, FSOSET, the 1st iteration MSST, the 1st iteration FMSST, the 8th iteration MSST and the 8th iteration FMSST methods of the bearing outer race DE fault position relative to load zone centered at 6:00 signals polluted by infinite variance process noise ($\alpha = 0.8$, $MSNR = 18$ dB, $p = 0.2$). The result of the fault diagnosis demonstrates that the existing synchrosqueezing and synchroextracting transform TFR methods can not work under infinite variance process environment, as shown in Fig. 17a,c,e,g,i. Hence, the traditional synchrosqueezing and synchroextracting methods are invalid. However, the fault diagnosis demonstrates that the improved synchrosqueezing and synchroextracting methods can successfully diagnose of the outer race DE fault position relative to load zone centered at 6:00 data contaminated by infinite variance process noise well in low $MSNR$, as shown in Fig. 17b,d,f,h,j. The results above indicate that the improved synchrosqueezing and synchroextracting TFR methods have better performance than the exiting methods, which

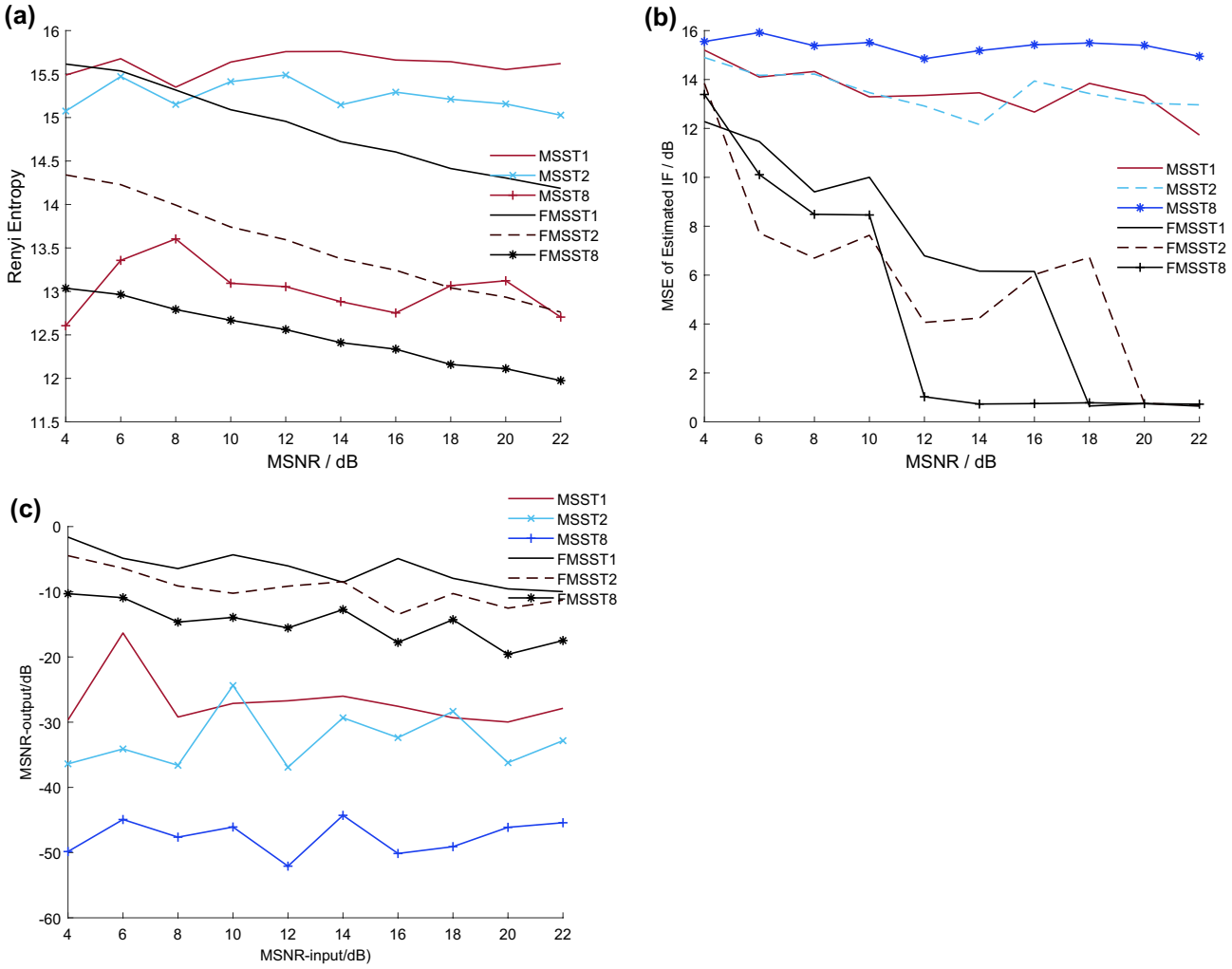

Figure 14. Renyi entropy, mixed *MSE*s of IF and *MSNR*—output comparisons of the Nth iteration MSST and FMSST methods under different *MSNR* ($\alpha = 0.8$). (**a**) Renyi entropy; (**b**) Mixed *MSE*s of IF; (**c**) *MSNR* —output).

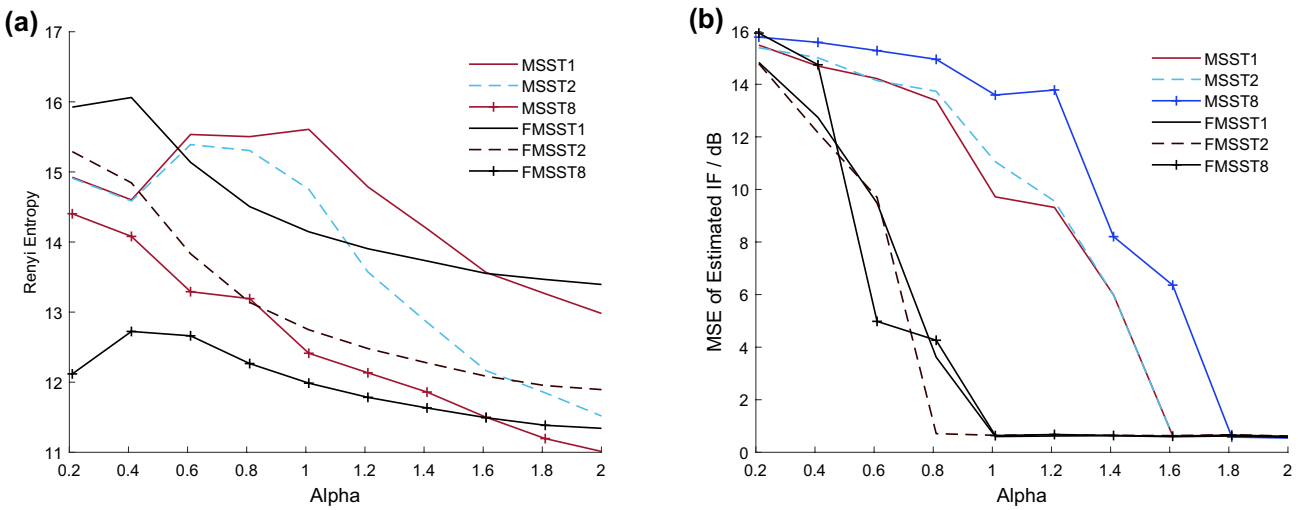

Figure 15. Renyi entropy and mixed *MSE*s of IF comparisons of the Nth iteration MSST and FMSST methods in different α ($MSNR = 16dB$). (**a**) Renyi Entropy; (**b**) mixed *MSE*s of IF).

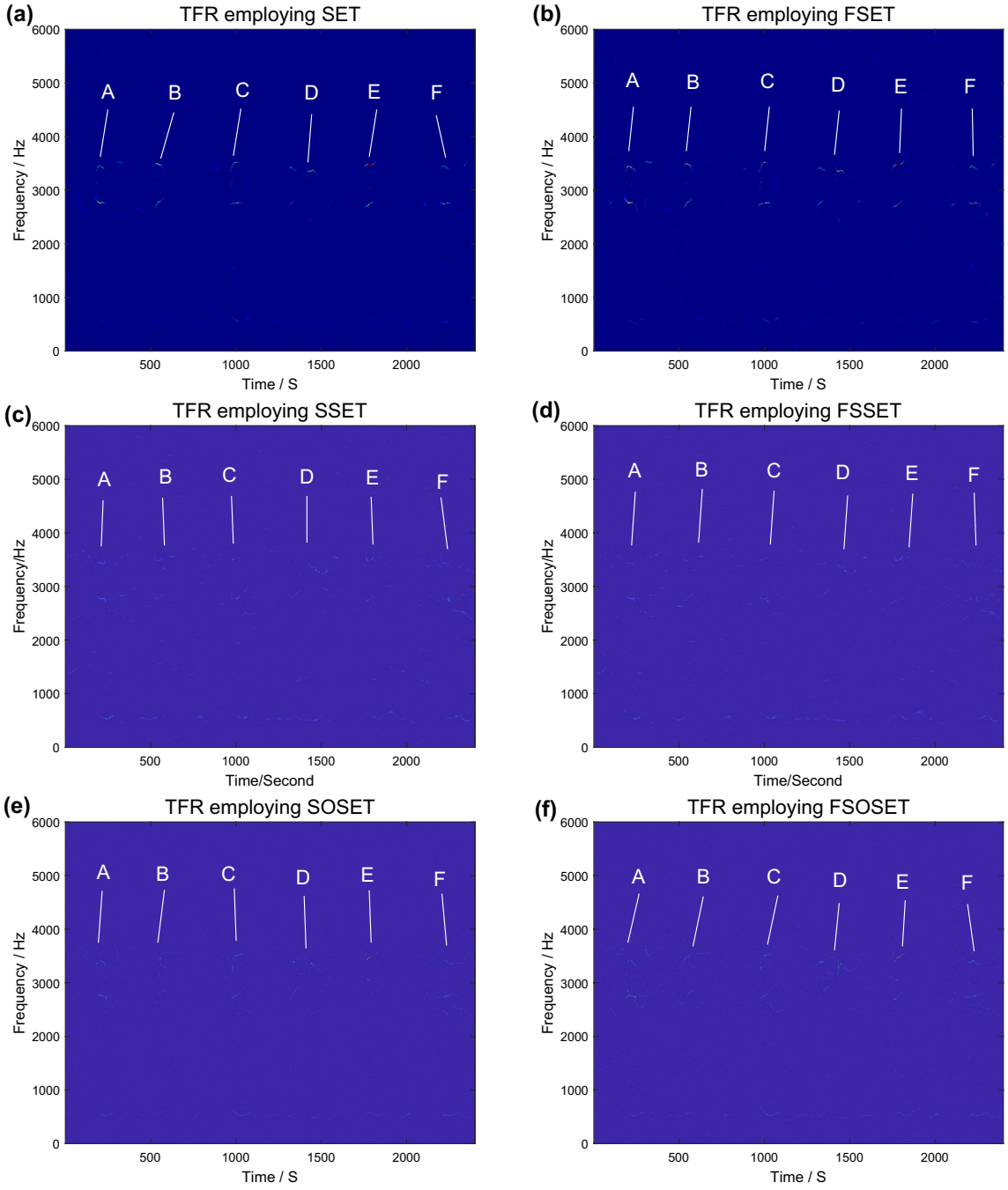

Figure 16. TFRs of the outer race DE fault signal polluted by infinite variance process noise ($\alpha = 2$, $SNR = 5$ dB, $p = 0.8$). (**a**) SET method. (**b**) FLOSET method. (**c**) SSET method. (**d**) FLOSSET method. (**e**) SOSET method. (**f**) FSOSET method. (**g**) The 1st iteration FMSST method. (**h**) The 1st iteration FMSST method. (**i**) The 8th iteration MSST method. (**j**) The 8th iteration FMSST method).

are robust, and they can be effectively applied to the bearing fault diagnosis of the rotor system in complex and harsh environment.

To prove the validity of the improved synchrosqueezing and synchroextracting TFR methods in bearing fault diagnosis and further verify their performance, we have done the following experiments ($K = 10$, $p = 0.4$) with the bearing outer race DE fault position relative to load zone centered at 6:00 data contaminated by infinite variance process noise ($\alpha = 1.0$) under different *GSNR* (4–22 dB), the Renyi Entropy, mixed *MSE*s of IFs combined with ridge extraction techniques and *MSNR*—output comparisons are shown in Fig. 18. Moreover, we let $MSNR = 18$ dB, $p = 0.4$, $K = 10$, and repeat the above the Renyi Entropy and mixed *MSE*s of IFs experiment for the improved synchrosqueezing and synchroextracting methods under different α (0.2–2), Fig. 19 shows that the result.

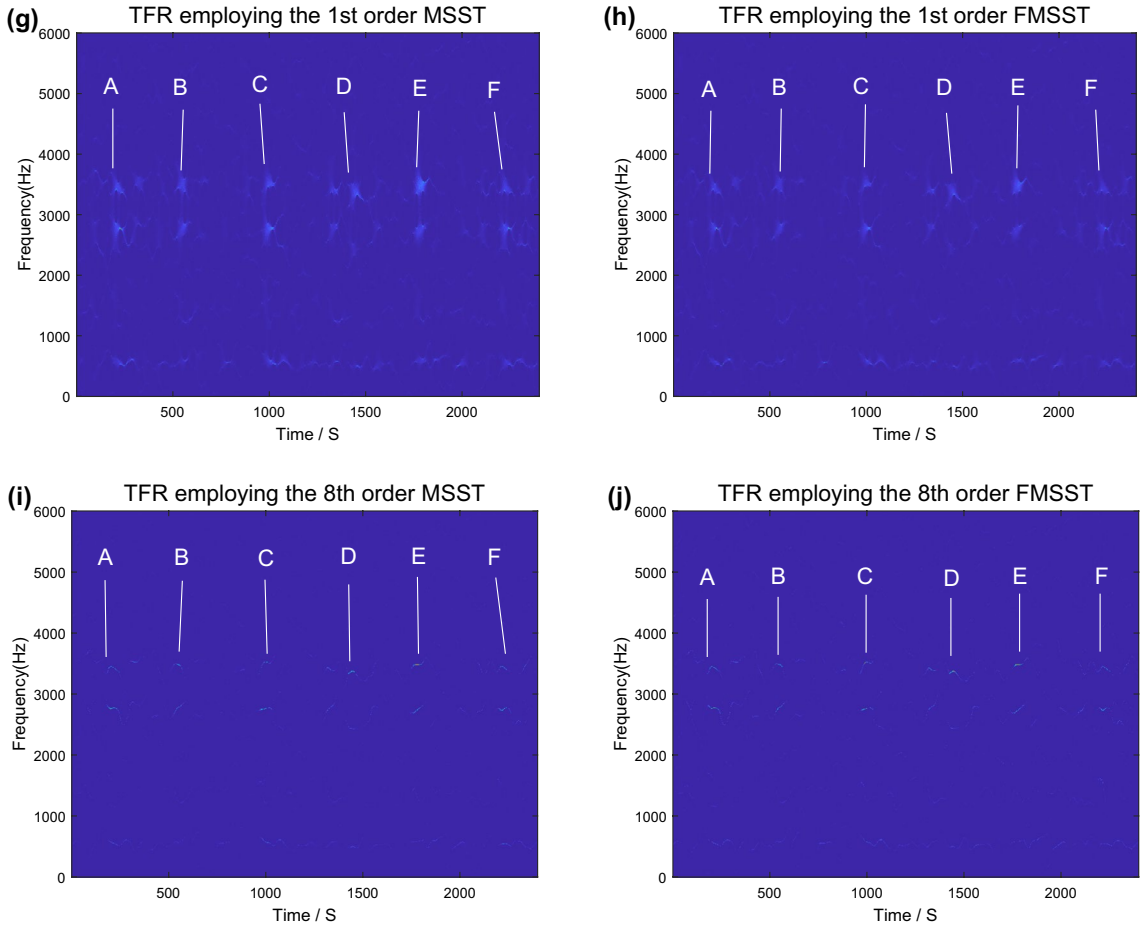

Figure 16. (continued)

Figure 18 shows that Renyi entropy, mixed *MSE*s of IF employing ridge extraction techniques and *MSNR*—output comparisons results of FSTFT time frequency representation, FSST time frequency representation, FSST2, FSET, FSSET, FSOSET, the 1st iteration FMSST and the 8th iteration FMSST methods of the bearing outer race DE fault position relative to load zone centered at 6:00 data contaminated by infinite variance process noise in different *MSNR* ($\alpha = 1.0$), respectively. It is clear that the FSTFT method has maximal Renyi entropy, and Renyi entropy of the 8th iteration FMSST method is the smallest. The FSST2 method has the smallest reconstruction error of the bearing outer race signal and the strongest noise suppression ability. The FSET and FSSET methods are limited by kernel function, and which are not effective in extracting fast-changing fault signals, resulting in large mixed *MSE*s of IFs reconstruction.

Figure 19 shows Renyi entropy of the 8th iteration FMSST method is optimal when characteristic index α changes from 0.2 to 2 and *MSNR* keeps in 18dB. When $\alpha > 0.8$, FSST, FSST2, FOSTFT, FMSST and FMSST8 employing the ridge extraction techniques have almost the same mixed *MSE*s of IF, hence, which have wider applicability and better performance than the others, and they have good toughness.

The features, deficiencies and application scenarios of the robust synchrosqueezing and synchroextracting TFR methods have been summarized in Table 2. The FSST method aims to improve the TF energy concentration by squeezing the fault signals' fuzzy energy in the FSTFT TF domain to IFs trajectory, the specific process is to apply IFs to gather the FSTFT TF points with the same frequency. Although the energy concentration of FSTFT time frequency representation can be improved, noise may be increased into the TFR of the fault signals during the squeezing process. Hence, the noise suppression ability of the FSST method is poor, and which has poor processing effect for strong time-varying signals.

In order to further verify the effectiveness of the improved method, we selected the bearing outer race fault data of Jiangnan University[30]. The sampling frequency of the data was 50 kHz, and the data of N = 5000 was taken as the test signal, so the time was 0.1 s and the bearing speed was 800 rpm/min. We applied the FSST, FSET, FSSET, FSOSET, the 1st iteration FMSST and the 8th iteration FMSST methods to demonstrate the TFRs of the pulse components under variable speed conditions, the simulation results are shown in Fig. 20. It can be seen that the TFRs can extract the pulse features at the same time interval, and the time interval of these continuous pulses A, B, C, D, E, F and G is about 14.28 ms, then the characteristic frequency can be calculated to be about 70 Hz. In summary, the proposed fractional low-order time–frequency techniques can effectively extract pulse characteristics of mechanical fault bearing signals in time–frequency domain under variable speed conditions, and accurately obtain the information closely related to the fault characteristics.

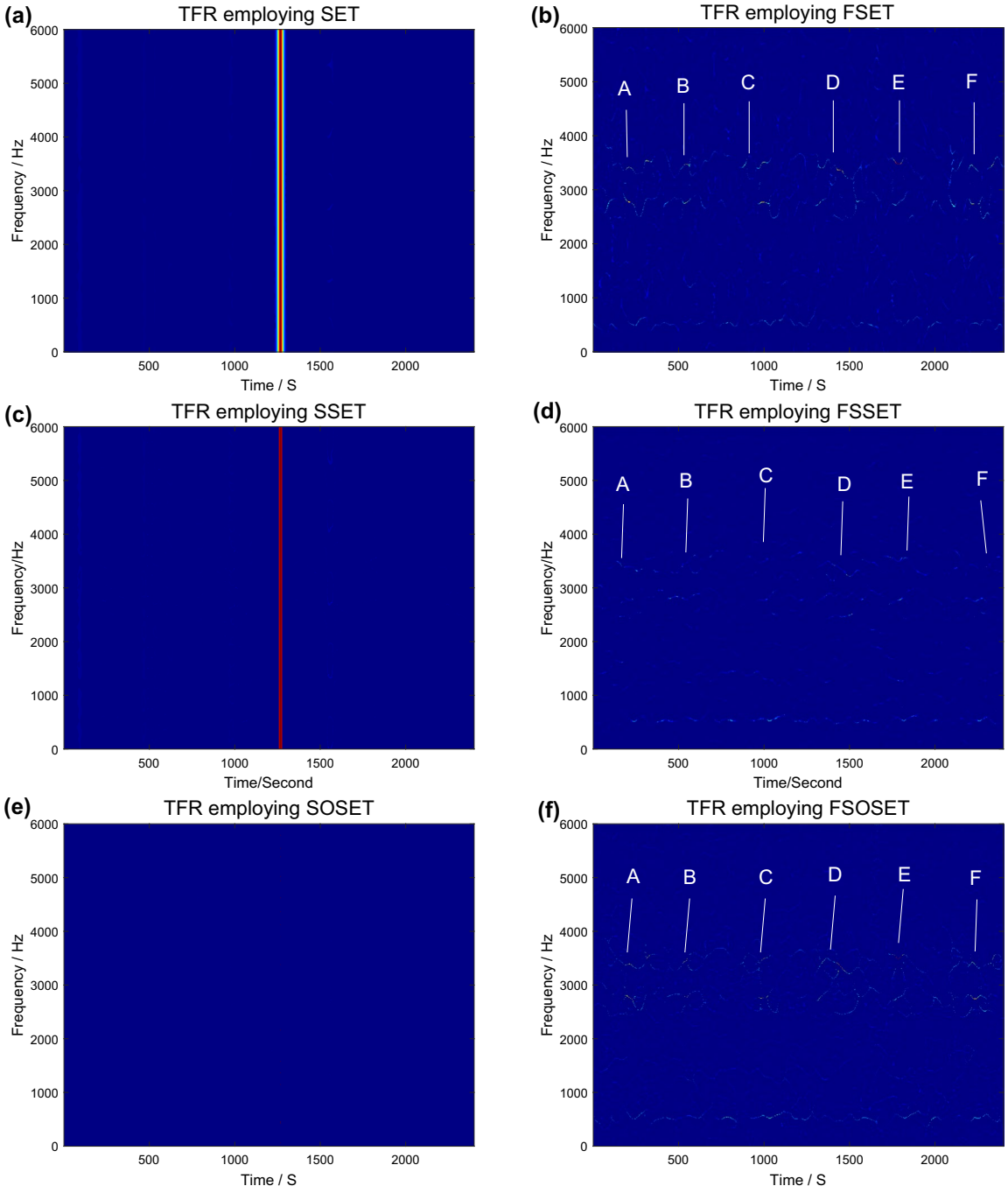

Figure 17. TFRs of the outer race DE fault signal polluted by infinite variance process noise ($\alpha = 0.8$, $MSNR = 18$ dB, $p = 0.2$). (**a**) SET method. (**b**) FSET method. (**c**) SSET method. (**d**) FSSET method. (**e**) SOSET method. (**f**) FSOSET method. (**g**) The 1st iteration MSST method. (**h**) The 1st iteration FMSST method. (**i**) The 8th iteration MSST method. (**j**) The 8th iteration FMSST method).

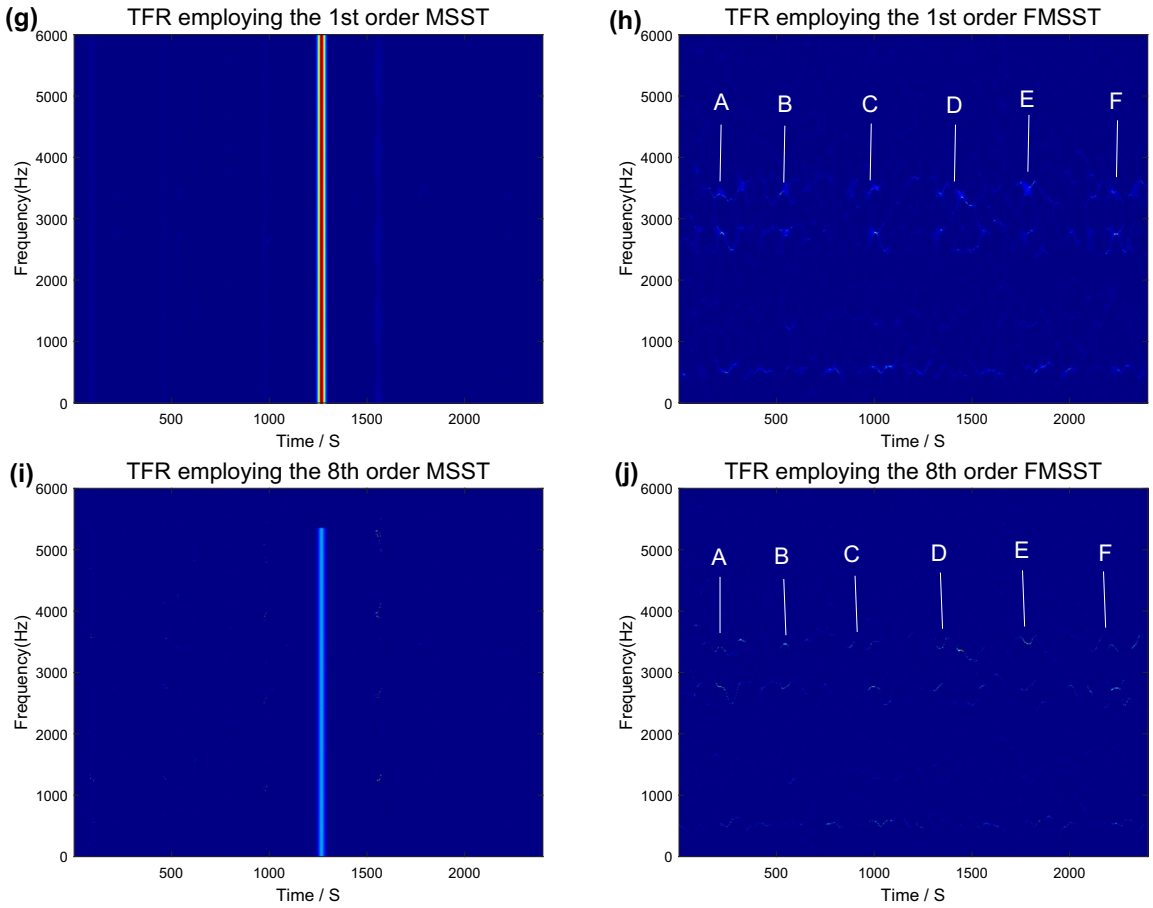

Figure 17. (continued)

The FSET method aims at the characteristics that some special points in FSTFT time frequency representation have the largest peak value, the energy peak on IF trajectory can be accurately located employing synchronous extraction operation (SEO), and new TF coefficient is obtained. The FSET method has good noise robustness, but limited by the kernel function, the extraction effect of TF is not good for the fast-changing fault signal, and the energy concentration is not high.

FSSET is a method based on the FSST and FSET, which uses FSST instead of FSTFT time frequency representation to extract the peak value of IF energy, and finally determines new TF coefficients. FSSET method has higher TF energy concentration and TF resolution than FSST and FSET, which has the advantages of both methods, good noise suppression ability (strong noise robustness) and fast algorithm speed (short algorithm time). FSSET removes many coefficients that are critical to characterizing m-D patterns, which produce blurred and ridged TF images. The FSST, FSET and FSSET methods are based on the Dirac signal model.

The FSOSET method is a FSTFT TF post-processing technology based on FGMLC model, which applies second-order synchronous extraction operation (FSOSEO) instead of FSEO to synchronize TFR of the fault signals, it further improves the energy concentration of TFR and reduces the reconstruction error. The FSOSET method can show time-varying non-stationary fault signals more accurately. FSOSET can have more focused TF images, better reversibility of TF representation, and stronger noise suppression (strong noise robustness). The Renyi entropy of the FSOSET method is inferior to that of the SOSET method.

FMSST method is based on FSST, and adopts iterative reassignment process to gradually concentrate fuzzy energy in the TF domain, thereby improving the energy concentration of TFR, while maintaining the TF reconstruction ability of the bearing fault signal. The FMSST method is suitable for the strong time-varying fault signals with less computation, and which can be applied to real-time signal processing. By employing iteratively multiple FSSO operations, the fuzzy energy in the FSST TF domain is gradually concentrated.

In practical application, we can choose the method suitable for fault diagnosis analysis according to the advantages and disadvantages of the algorithm and the characteristics of the fault signal itself, and we can also synthesize several methods for joint fault diagnosis.

Conclusions

In this paper, infinite variance process statistical model has been used to describe the normal signal, DE fault vibration signal, and environmental noise. The characteristic index α of the inner race and outer race fault signal in DE and FE is less than 2. Aiming at degradation of the exiting methods in infinite variance process environment, several robust post-processing synchrosqueezing and synchroextracting TFR technologies were proposed

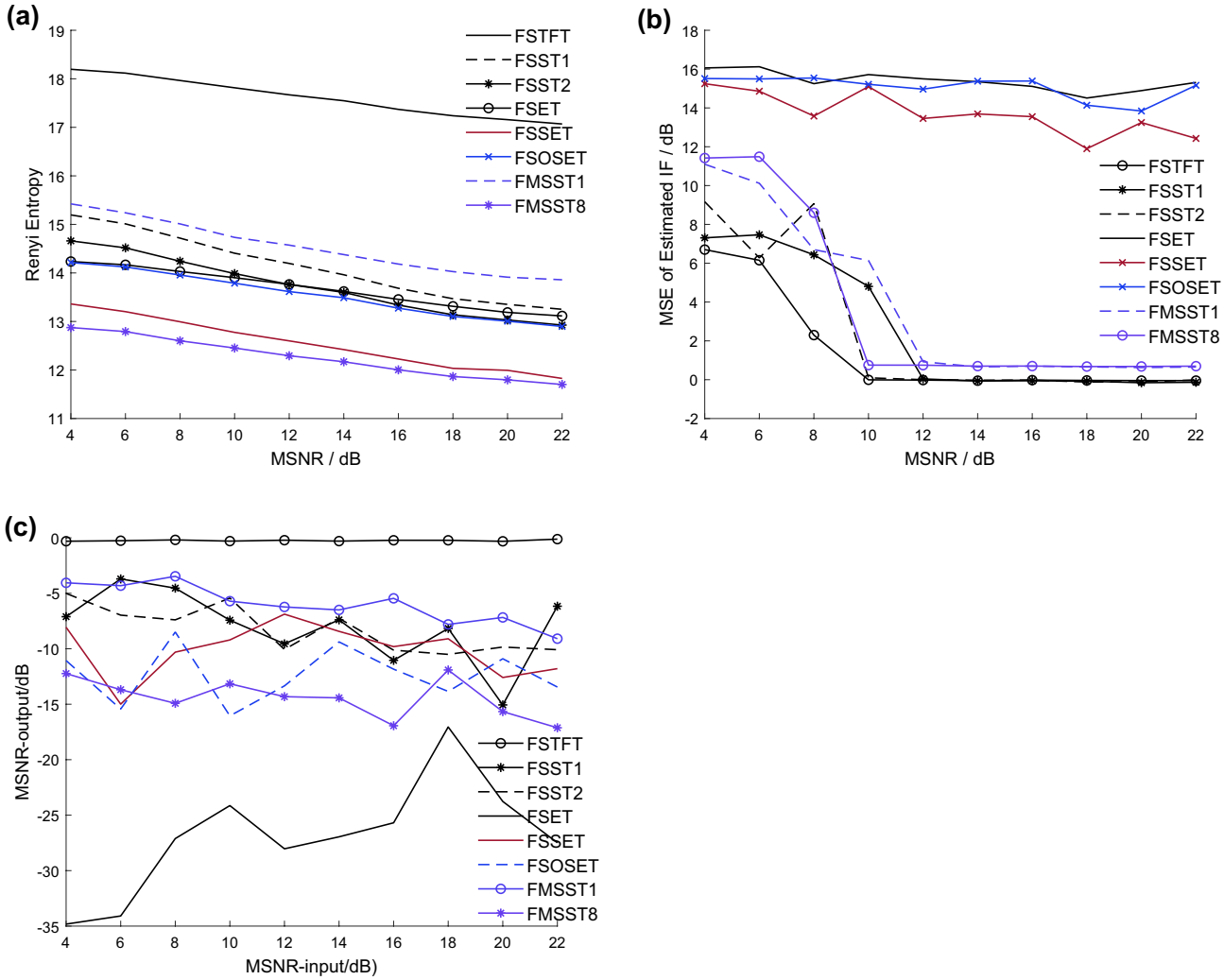

Figure 18. Renyi Entropy, mixed *MSE*s of IF and *MSNR*—output comparisons of of IF estimation of outer race DE fault signals employing FSTFT, FSST, FSET, FSSET, FSOSET, the 1st iteration FMSST and the 8th iteration FMSST methods under different *MSNR* ($\alpha = 1.0$). (**a**) Renyi Entropy; (**b**) Mixed *MSE*s of IF; (**c**) *MSNR*—output.

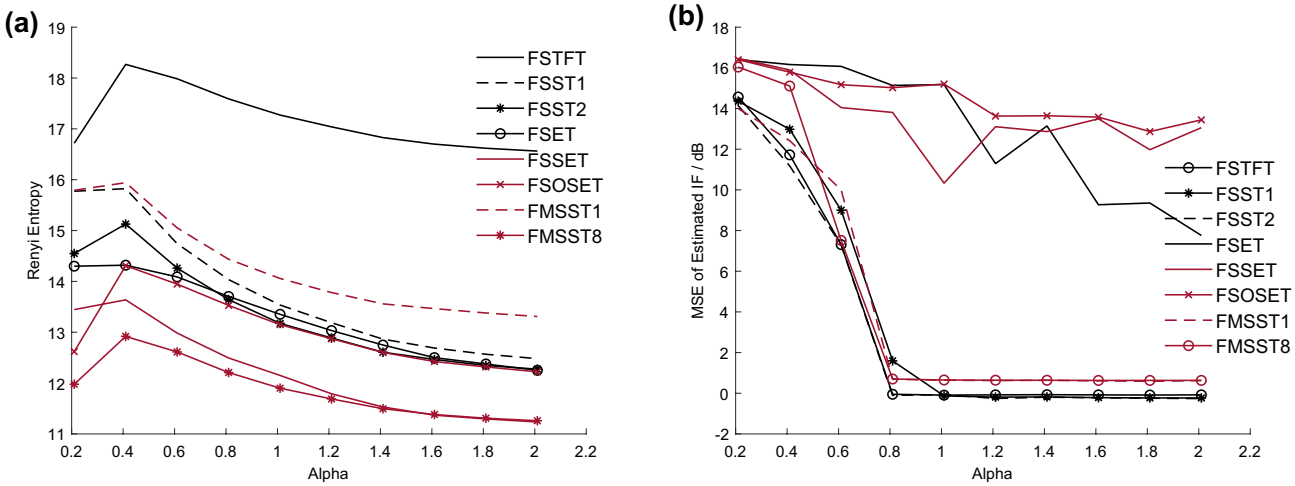

Figure 19. Renyi entropy and mixed *MSE*s of IF estimation of outer race DE fault signals employing FSTFT, FSST, FSET, FSSET, FSOSET, the 1st iteration FMSST and the 8th iteration FMSST methods in different α (*MSNR* = 18 dB). (**a**) Renyi entropy; (**b**) Mixed *MSE*s of IF.

Methods	Features	Deficiencies	Application scenarios
FSTFT	Low computational complexity and balanced TF resolution	The overall time–frequency aggregation of the signal is low	Preliminary analysis for fault signal
FSST	It can improve the energy concentration of FSTFT time frequency representation through the synchrosqueezing process	Poor noise suppression ability	The processing effect of strong time-varying fault signal is poor as post-processing method
FSET	The energy concentration of FSTFT time frequency representation is improved by the synchroextracting process	Good noise robustness but limited by kernel function	TF extraction effect and the energy concentration of fault signal are undesirability
FSSET	It has higher TF energy concentration and TF resolution than FSST and FSET	It has the advantages of both FSST and FSET methods	Fault signal TF images with blurred and ridged fractures are produced
FSOSET	Replace synchroextracting operation with second-order synchroextracting operation	Strong noise suppression ability	It has a more concentrated TF image of fault signals and better reversibility
FMSST	By iterating FSSO operations several times, FSSO fuzzy energy in TF domain is gradually concentrated	Less computation, improving the energy concentration of TFR while maintaining the signal TF reconstruction capability	It is suitable for strong time-varying fault signals, and can be applied to real time fault analysis

Table 2. The comparison of various robust synchrosqueezing and synchroextracting transform TFR methods.

including FSST, FSET, FSSET, FSOSET and FMSST algorithms. The robust post-processing TFR technologies have wider applicability and better signal TF aggregation than the conventional technologies. FSST method is to adjust the TF coefficient of IF to improve its TF concentration. The FSET method can accurately locate the energy peak of IF trajectory to obtain new TF coefficients. The FSSET method extracts the IF energy peak from the FSST TF domain to determine the new TF coefficient. The FSOSET algorithm uses second-order synchronous extraction operation to extract synchronously in FSTFT TF domain, which has good TF reversibility and strong noise robustness. The FMSST method uses iterative reassignment technique to gradually concentrate fuzzy energy. The robust post-processing time frequency technologies have smaller Renyi Entropy and mixed *MSE* of IF, and larger *MSNR*-output. In the actual fault analysis and diagnosis, the suitable method can be selected based on the characteristics and advantages of the above the robust post-processing TFR technologies, and even a variety of technologies can be jointly discussed to obtain better diagnosis results. The improved post-processing algorithm in this paper adopts a fixed parameter P and has certain application limitations. In the next step, we will study the adaptive improvement of these algorithms.

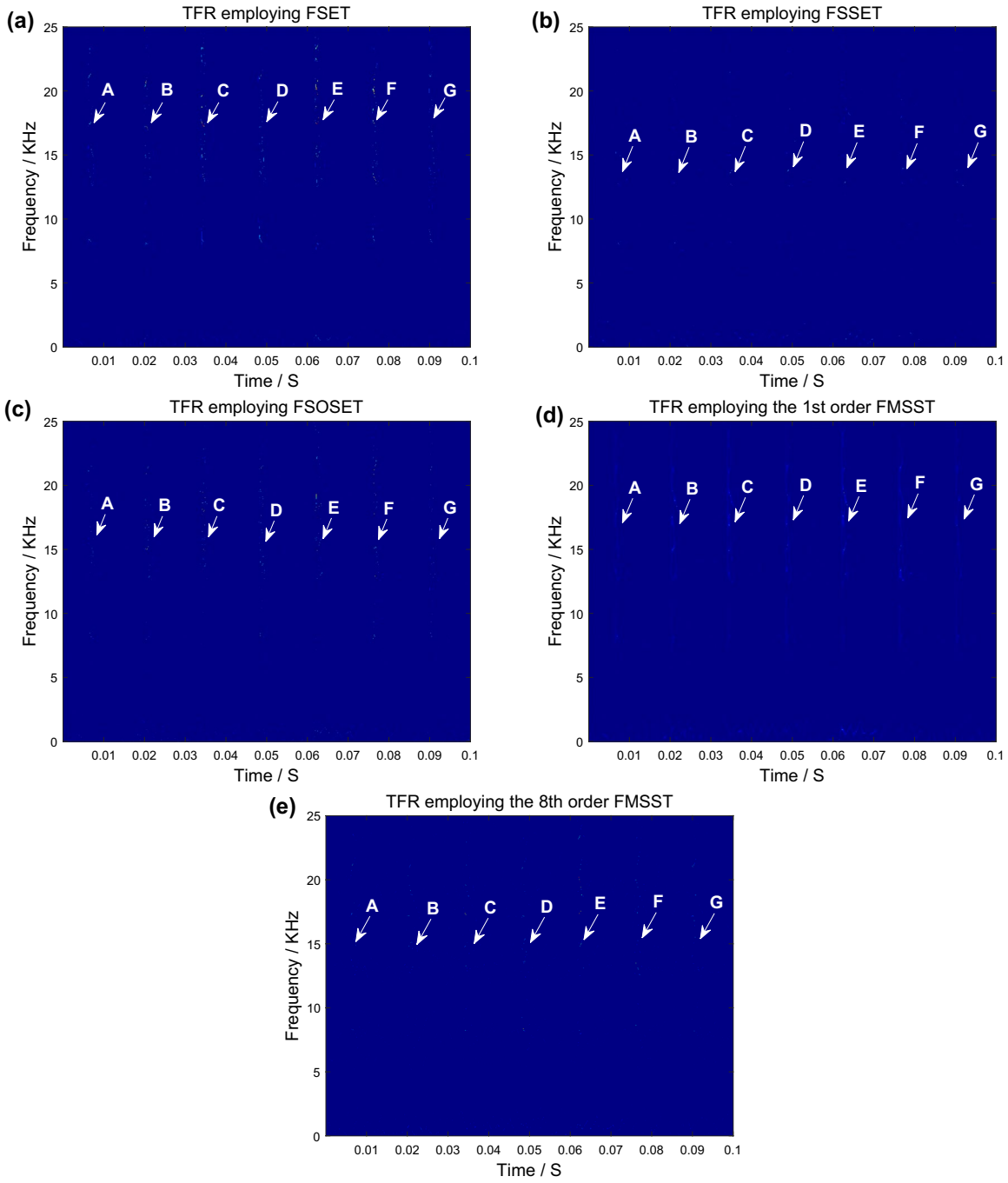

Figure 20. TFRs of the outer race bearing fault signal employing FSET, FSSET, FSOSET, the 1st iteration FMSST and the 8th iteration FMSST methods. (**a**) FSET method. (**b**) FSSET method. (**c**) FSOSET method. (**d**) The 1st iteration FMSST method. (**e**) The 8th iteration FMSST method.

Data availability

The authors confirm that the data supporting the findings of this study are available within the article and its supplementary materials.

Received: 6 May 2024; Accepted: 14 August 2024
Published online: 03 September 2024

References

1. Shreyas, G. *et al.* Multi-fault diagnosis of industrial rotating machines using data-driven approach: A review of two decades of research. *Eng. Appl. Artif. Intell.* **123**, 106139 (2023).
2. Benjemaa, R., Elhsoumi, A. & Abdelkrim, M. N. Fault diagnosis and fault-tolerant control design for neutral time delay system. *Automatica* **64**(3), 422–430 (2023).

3. Liu, X. Y. & He, Y. G. A multi-stream multi-scale lightweight SwinMLP network with an adaptive channel-spatial soft threshold for online fault diagnosis of power transformers. *Meas. Sci. Technol.* **34**(7), 075014 (2023).
4. Liu, W., Liu, Y., Li, S. & Zhai, Z. Demodulated synchrosqueezing S-transform and its application to machine-fault diagnosis. *Meas. Sci. Technol.* **34**(6), 065004 (2023).
5. Luczak, D., Brock, S. & Siembab, K. Cloud based fault diagnosis by convolutional neural network as time-frequency RGB image recognition of industrial machine vibration with internet of things connectivity. *Sensors* **23**(7), 3755 (2023).
6. Chen, J., Hao, L., Li, H. & Zhang, L. Time-frequency characteristics analysis and diagnosis of rotating rectifier faults in multiphase annular brushless system. *IEEE Trans. Ind. Electron.* **70**(4), 3233–3244 (2023).
7. Wei, D. Y. & Shen, J. S. Multi-spectra synchrosqueezing transform. *Signal Process.* **207**, 108940 (2023).
8. Shi, J., Chen, G., Zhao, Y. N. & Tao, R. Synchrosqueezed fractional wavelet transform: A new high-resolution time-frequency representation. *IEEE Trans. Signal Process.* **71**, 264–278 (2023).
9. Chen, X. P., Chen, H., Hu, Y., Xie, Y. T. & Wang, S. Y. A sparse time-frequency reconstruction approach from the synchroextracting domain. *Signal Process.* **222**, 109517 (2024).
10. Gorur, K., Olmez, E., Ozer, Z. & Cetin, O. EEG-driven biometric authentication for investigation of Fourier synchrosqueezed transform-ICA robust framework. *Arab. J. Sci. Eng.* **48**(8), 10901–10923 (2023).
11. Liu, C. A. *et al.* Dual-FBG bearing fault probe based on a CNN-LSTM-encoder network. *Appl. Opt.* **62**(8), 1984–1991 (2023).
12. Lv, Y., Wu, H. A., Yuan, R., Dang, Z. & Song, G. B. Generalized synchroextracting-based stepwise demodulation transform and its application to fault diagnosis of rotating machinery. *IEEE Sens. J.* **23**(5), 5045–5060 (2023).
13. He, T., Peng, S. P. & Geng, H. G. Local maximum second order multi-synchrosqueezing transform for high resolution surface-wave group velocity dispersion energy imaging. *IEEE Geosci. Remote Sens. Lett.* **21**, 7503405 (2024).
14. Hao, G. C. *et al.* Second-order transient-extracting generalized warblet transform optimized by FrVMD. *IEEE Trans. Ind. Electron.* **71**(8), 9500–9509 (2024).
15. Tan, C. J., Zhao, H., OBrien, E. J., Uddin, N. & Kim, C. W. Exploring time-varying characteristics in drive-by bridge frequency extraction with the second-order synchrosqueezing transform. *J. Bridge Eng.* **28**(4), 04023010 (2023).
16. Cheng, Q., Cui, F., Dong, G. Q., Wang, R. & Li, S. A method of reconstructing ground penetrating radar Bscan for advanced detection based on high-order synchrosqueezing transform. *IEEE Trans. Geosci. Remote Sens.* **62**, 5910313 (2024).
17. Wang, X. K., Liu, D. W., Chen, W. C. & Li, C. A cascaded synchrosqueezing transform for precise analysis of seismic signal. *IEEE Trans. Geosci. Remote Sens.* **62**, 5901912 (2024).
18. Wei, D. H. *et al.* Iterative rounded transient-synchrosqueezing-extracting transform and its application. *IEEE Trans. Ind. Electron.* **70**(10), 10567–10577 (2023).
19. Liu, W., Liu, Y., Zhai, Z. X. & Li, S. X. Time-reassigned multisynchrosqueezing S-transform for bearing fault diagnosis. *IEEE Sens. J.* **23**(19), 22813–22822 (2023).
20. Chen, S. Y., Xue, Y. J. & Huang, L. Application of second order multi-synchrosqueezing transform for seismic data analysis. *Dig. Signal Process.* **148**, 104436 (2024).
21. Yu, G., Huang, X. G., Lin, T. R. & Dong, H. R. A non-linear time-frequency tool for machinery fault diagnosis under varying speed condition. *Mech. Syst. Signal Process.* **186**, 109849 (2023).
22. Ying, W. M. *et al.* Order-frequency Holo-Hilbert spectral analysis for machinery fault diagnosis under time-varying operating conditions. *ISA Trans.* **146**, 472–483 (2024).
23. Guo, W. Y. & Zhi, Y. F. Nonlinear spline versoria prioritization optimization adaptive filter for alpha-stable clutter. *IEEE Trans. Aerospace Electron. Syst.* **59**(1), 734–744 (2023).
24. Mesropyan, M. T. & Bardakhchyan, V. G. Hellinger's distance and correlation for a subclass of stable distributions. *J. Contemp. Math. Anal. Armenian Acad. Sci.* **58**(3), 191–195 (2023).
25. Tong, J. Y., Zhang, Z. H., Chen, Y. Q. & Zhang, Z. Z. Long time behaviour for population model by alpha-stable processes with Markov switching. *Nonlinear Anal. Hybrid Syst.* **50**, 101386 (2023).
26. Sathe, A. M., Upadhye, N. S. & Wylomanska, A. Forecasting of symmetric -stable autoregressive models by time series approach supported by artificial neural networks. *J. Comput. Appl. Math.* **425**, 115051 (2023).
27. Cui, W. C. *et al.* Dual-channel two-dimensional stochastic resonance and its application in bearing fault detection under alpha-stable noise. *Chin. J. Phys.* **88**, 922–937 (2024).
28. Long, J. B., Wang, H. B., Fan, H. S. & Lao, Z. W. Applications of improved linear chirplet time frequency representation to machine bearing fault analysis. *Measurement* **209**, 112460 (2023).
29. *CWRU Bearing Data Center*. https://csegroups.case.edu/bearingdatacenter/pages/download-data-file.
30. *The Bearing Outer Race Fault Data of Jiangnan University*. http://www.52phm.cn/datasets/bear/Bearing-data-set-of-Jiangnan-University.html.

Acknowledgements

This work was supported by Science and Technology Project of Jiangxi Provincial Health Commission (202211976), Science and Technology Project of Jiangxi Provincial Department of Education (GJJ2201906).

Author contributions

Junbo Long and Changshou Deng wrote the main manuscript text and Haibin Wang prepared the figures. All authors reviewed the manuscript.

Funding

This work was supported by Science and Technology Project of Jiangxi Provincial Health Commission (202211976), Science and Technology Project of Jiangxi Provincial Department of Education (GJJ2201906).

Competing interests

The authors declare no competing interests.

Additional information

Correspondence and requests for materials should be addressed to C.D.